

1 ICE-CAMERA: a flatbed scanner to study inland Antarctic polar precipitation.

2
3 Massimo Del Guasta

4 Istituto Nazionale Ottica CNR, Sesto Fiorentino, 50019, Firenze, Italy

5 *Correspondence to:* Massimo Del Guasta (massimo.delguasta@ino.cnr.it)

6 **Abstract.**

7 Studying precipitation at very high latitudes is difficult because of the harsh environmental conditions that limit the external
8 activity of humans and instruments, especially in the polar winter. The direct monitoring of ice crystal habits and size
9 distribution in antarctic precipitation is important for the validation of the algorithms used for retrieving precipitation from
10 ground-based and satellite-borne radar instruments, and for the improvement of the climatological modeling of polar areas.
11 The paper describes an automated device (ICE-CAMERA) specifically developed for the imaging, measurement and
12 classification of ice precipitation on the Antarctic high plateau. The instrument gives detailed information on precipitation on
13 an hourly basis. The article provides a description of the device and its image processing software. Starting in 2014, the
14 instrument operates *almost* unattended all year round at Concordia station, Antarctica (75°S, 123°E, 3220 m altitude).

16 **1. Introduction.**

17 In Antarctica, the characteristics of ice precipitation depend greatly on the region. In coastal areas, precipitation is influenced
18 by synoptic scale features, such as cyclones and fronts (Bromwich, 1988). In the interior (> 2500 m), a significant part of the
19 precipitation falls in the form of small ice crystals (“diamond dust”, DD) under clear-sky conditions (Fujita and Abe, 2006).
20 Snow particles over Antarctica are generally smaller compared to other regions of the world. The largest particles are found
21 close to the coast, where more water vapour is available and diameters up to 10 mm are recorded (Konishi et al., 1992) with
22 particle shapes similar to mid-latitude ones (Satow, 1983). More inland stations record snowflakes of much smaller sizes,
23 ranging from particles smaller than 100 μm at South Pole (Walden et al., 2003, Lawson et al., 2006) till hundreds of μm at
24 other inland stations (Lachlan-Cope et al., 2001).

25 In situ measurements of precipitation are rare in Antarctica and affected by large uncertainties. This is particularly true in the
26 high plateau, where less than 20 cm of snow accumulates every year (Palermo et al., 2014). As a result, the global precipitation
27 products that rely on these observations (i.e. the Global Precipitation Climatology Centre (GPCC), (Schneider et al., 2017))
28 have no coverage over this region. Other observational products, such as the Global Precipitation Climatology Project (GPCP)
29 (Huffman et al 2001), that uses GPCC for bias correction over land, has relied on satellite-only precipitation estimates. Satellite
30 products also face large uncertainties over cold regions such as Antarctica due to insufficient sensitivity of sensors to detect
31 and estimate precipitation signals, complex surface emissivities, and poor understanding of precipitation microphysics. Ground
32 based K-band radars (~1-cm wavelength) are robust instruments successfully employed for studying precipitation in coastal
33 Antarctic sites (Souvereinjs et al., 2017) but are quite blind to the sub-millimetre ice particles encountered on the plateau, due
34 to the relationship D^6 between the radar scattering cross-section and the particle diameter (D).

35 The satellite-borne radar CloudSat (Liu, 2008) did provide a quantum leap in observing ice in the Antarctic atmosphere (up
36 to 82 °S), but being a single-frequency radar (like K-band radars), the retrieval of precipitation quantities relies on many
37 assumptions about the properties of particles, resulting into $\pm 50\%$ uncertainties for IWC (Heymsfield et al., 2008). The
38 microphysical assumptions (shapes and size distribution of particles) are the biggest causes for IWC, IWP, and snowfall rate
39 retrieval uncertainty (Hiley et al., 2011, Wood et al., 2015). Moreover, CloudSat bins close to the ground cannot be used for
40 precipitation retrieval, resulting into a severe underestimation of the diamond-dust and blowing-snow contribution to Antarctic
41 snow balance (Palm et al., 2018). Despite these uncertainties, in absence of ground validation CloudSat data are now used as
42 independent data set for the validation of precipitation models in Antarctica (Palermo et al., 2014, Palermo et al., 2017).

43 The direct observation and the continuous monitoring of habit and size distribution of precipitation is therefore required in
44 order to validate both precipitation models, CloudSat and radar algorithms on the Antarctic plateau.

45 Disdrometers are robust *in-situ* devices, increasingly used in Antarctic coastal areas (Bracci et al.,2022). They provide the
46 size distribution and falling speed of hydrometers, but they give no direct information about the shape. The evolution of
47 disdrometers into 2D-disdrometers gave access to some shape indications about hydrometeors (Grazioli et al.,2014). A further
48 evolution of disdrometers into Imaging-disdrometers, such as the Snowflake Video Imager (SVI) (Newman et al., 2009),
49 provided realistic images of the crystals. Grazioli et al., (2017), as part of a multidisciplinary field campaigns, deployed a
50 multi-angle snowflake camera (MASC) to take photographs of individual snow particles. This instrument, representing a
51 further advance in the field of imaging disdrometers, collects high-resolution stereoscopic photographs of snowflakes in free
52 fall while they cross the sampling area (Garrett et al., 2012), thus providing information about snowfall microphysics (Praz et
53 al., 2017). The optical structure of the imaging-disdrometer and the MASC makes these instruments reliable in the presence
54 of millimetre-sized hydrometeor precipitation. In Antarctica, their practical application is mainly limited to coastal areas.

55 The direct observation of inner Antarctic particles requires imaging techniques with resolution of a few microns. Photographic
56 studies of precipitation in the interior of the Antarctic are quite rare, carried out primarily at the South Pole Station (SPS)
57 through formvar replicas. In early works with formvar, Hogan (1975) identified at SPS millimetre-sized columnar crystals and
58 column- and bullet-rosettes in cloud precipitation, and smaller ($\approx 100 \mu\text{m}$ diameter) platelike particles in clear-sky
59 precipitation. Satow (1983), working with formvar replicas on Mizuho plateau found prevalently single bullets and
60 combination of bullets. Long solid column crystals were also found (with an air temperature range from -42°C to -56°C) with
61 a mean length of $290 \mu\text{m}$ and a maximum length of 1.2 mm , with a mean aspect ratio of 18. Small ($50\text{-}400 \mu\text{m}$) hexagonal,
62 triangular, scalene and square plates were also observed. Kikuchi and Hogan (1979) collected formvar replicas of DD in the
63 summer at SPS, finding columnar crystals of $90 \mu\text{m}$ average lengths and plates as small as $50 \mu\text{m}$ in diameter. Ohtake and
64 Yogi (1979) classified winter ice crystal precipitation in Antarctica under six categories. These included large rosettes, bullets
65 and columns (millimetre-sized), thin hexagonal plates and columns ($200 \mu\text{m}$ or less), and smaller crystals of various shapes
66 including triangular and polyhedral. Shimizu (1963) observed "long column" crystals in the winter at Byrd Station (80S,
67 120W). Size distributions of Antarctic DD in winter and spring were reported by Smiley et al. (1980) for particles larger than
68 $50 \mu\text{m}$: they observed the same ice crystal forms that were reported earlier. Walden et al. (2003) studied DD, blowing snow,
69 and cloud precipitation in winter, at SPS, by collecting crystals on slides and analyzing them using microphotography. In their
70 study, columns with an average length of $60 \mu\text{m}$ and plates with an average diameter of $30 \mu\text{m}$ were found in DD. The direct
71 observation of ice precipitation on the plateau was typically carried out by means of formvar replicas and/or
72 microphotography, but these techniques take time, are difficult to implement throughout the year and are necessarily limited
73 to short field campaigns and samples of very limited size. Designing automatic instruments for the continuous, photographic
74 study of precipitation in such a harsh environment necessarily require several compromises between the high resolution of
75 microphotography and the robustness of outdoor optical instruments such as disdrometers. Lawson et al. (2006) worked at
76 SPS, in summer, using innovative Cloud Particle Imagers (CPIs), which replaced formvar replicas. This technique allowed the
77 automatic analysis of around 700,000 DD crystal images in terms of caliper size, aspect ratio and other shape parameters. An
78 automatic classification software, based on shape parameters, was used to categorize the images into nine simplified classes:
79 small plates and spheroids, columns, thick plates, plates, budding rosettes, rosettes, complex with side planes, irregulars.

80 Concordia International Station, located on the Dome-C (DC, 75°S , 123°E , 3220 m above sea level) is a special location to test
81 new instruments for precipitation studies. Surface temperatures seldom exceed -25°C in summer, whereas winter temperatures
82 can reach -85°C . The 3 m average wind speed is 3 ms^{-1} for Aristidi (2005) and 4.5
83 ms^{-1} (hourly-averaged) for Argentini et al. (2014). The strongest winds (up to 15 ms^{-1} , hourly-averaged) blow from the
84 continental regions. These winds are due to gravity flows from the inner plateau regions south of Dome C, and are more often
85 observed during the winter, especially in coincidence with warming events. The circulation at the surface during the summer

86 is affected, especially in daytime, by the synoptic circulation. In summer the wind speed oscillates during the day, with values
87 increasing (by a few ms^{-1}) in the afternoon, when a convective layer develops, leading to the increase of the wind speed
88 (Argentini et al., 2014). Relative humidity relative to ice is typically around 55-85% (Genthon et al., 2022). In these conditions,
89 precipitation of ice crystals can be studied by simply collecting them on horizontal surfaces. This is done at DC by hand,
90 starting in 2008, collecting precipitation on flat surfaces ("benches") and visually inspecting it. This analysis is restricted to
91 one observation per day, a rate that is difficult to increase, especially in winter. The analysis of these samples is also time-
92 consuming and often subject to biases due to ice re-processing and sublimation, hoar formation, and subjective judgement of
93 the shape and relative abundance of ice particles. Schlosser et. al (2017) relied on this manual observation and classification
94 of ice particles in his analysis of precipitation isotope data at DC. They classified the ice grains into diamond dust, drifting
95 snow, snow and frost (hoar). The prevalence of hoar in the observed daily precipitation record (with temperatures below -
96 50°C) indicates the limitations of this manual technique if detailed information on DC precipitation particles is desired.

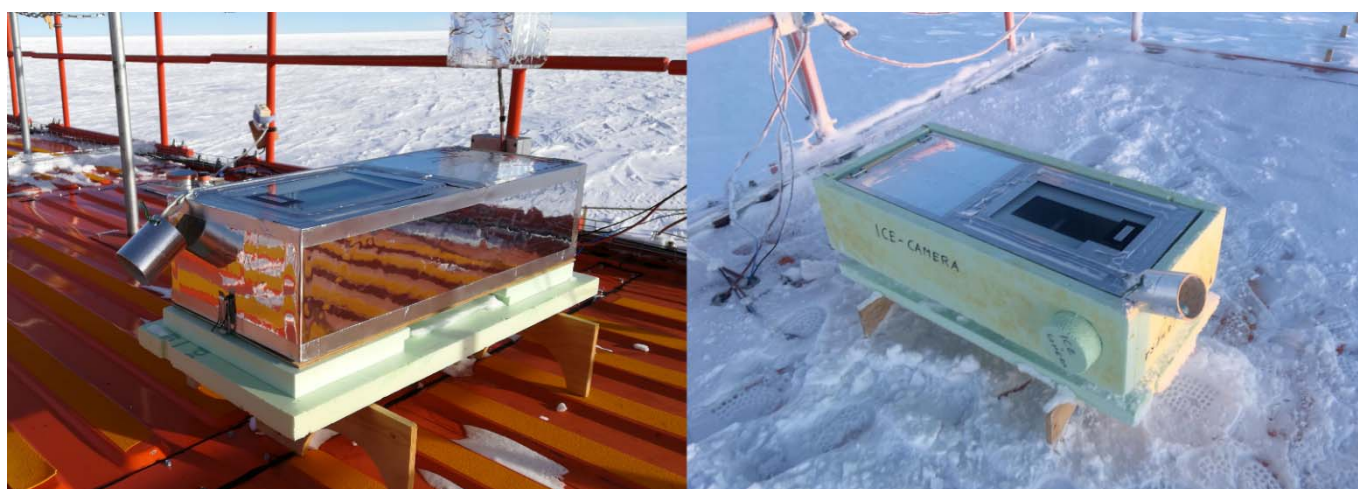
97 Detailed work was carried out in DC on a few individual DD and cloud precipitation crystal replicas by means of SEM electron
98 microscopy by Santachiara et al. (2016). They also analyzed very small particles (10-50 μm), in a size range inaccessible to
99 ordinary optical methods.
100 The purpose of developing ICE-CAMERA was to fill a gap in precipitation monitoring at Concordia with a robust instrument
101 capable of monitoring with continuity, all-year round, habit and size of ice particles in precipitation, while avoiding some of
102 the problems associated with the visual inspection of precipitation. This was achieved through the combined development of
103 robust camera equipment and machine learning techniques for sizing and classifying ice crystals.

104
105
106
107

108 2.1 Overview of the instrument.

109 ICE-CAMERA is a flatbed scanner (Zheleznyak et al, 2015), whose operating principle is the same as that of ordinary
110 flatbed scanners in offices. In the case of ICE-CAMERA, it specially designed for observing polar precipitation in the harsh
111 environmental conditions of Concordia station (Fig. 1). Within this work, the term "precipitation" will include both
112 "diamond dust" and cloud precipitation.

113
114

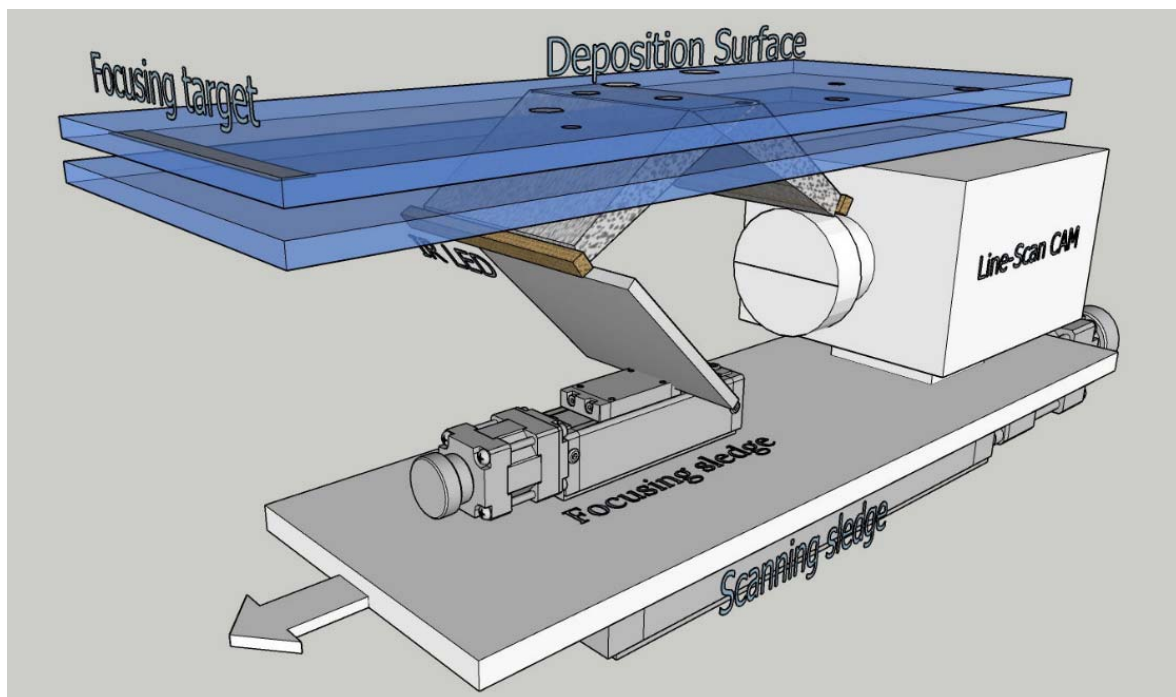


115
116
117
118

Fig. 1: ICE-CAMERA with its summer sun-shield (left) and with the winter coat (right).

119 The principle is simple: at the low temperatures and low wind speeds encountered at DC, precipitation falling on a horizontal
 120 glass surface accumulates with time until it sublimates, leaving plenty of time for scanning the glass surface for counting and
 121 measuring individual ice particles. The scanning, like in ordinary flatbed scanners, is performed by means of a line-scan camera
 122 (Sect.2.2), moved by a motorized scan sledge, and looking up at the DS through a 45° mirror (Fig. 2). The focus of the camera
 123 is adjusted by a small motorized focusing sledge moving the 45° mirror (Sect.2.3). During the scan, the image is sent to the
 124 PC, located inside the shelter.
 125 After a complete scan of the DS, the glass is heated and the precipitation sublimated (section 2.7). Once cooled down, the
 126 clean SD begins to accumulate new particles. This cycle takes place every hour. After each image acquisition, the MATLAB
 127 image processing code is called to process the DS image, and a summary-image containing only segmented particles (if
 128 present) is stored for post-processing. (Sect. 4.1.3). Every particle is also automatically measured through image processing
 129 (Sect. 4.1) and classified through machine learning (Sect.4.2). Individual particle data are stored in rows in a text file, along
 130 with weather and housekeeping data, for post-processing and statistical analysis.

131



132

133 **Fig. 2: ICE-CAMERA basics: the scan sledge moves the image-acquisition line along the deposition surface. The focusing sledge**
 134 **adjusts the focus.**

135

136 All basic operations of ICE-CAMERA, (with the exception of CAM acquisition) are driven by a custom microprocessor
 137 (Microchip PIC) logic board (Fig. 3). The same PIC board reads the housekeeping temperature sensors (attached to the DS
 138 and placed inside and outside the instrument), drives the stepper motors of the sledges as well as pumps and fans. The PIC
 139 Board communicates with the main computer (located inside the shelter) through RS232. NI Labview software controls image
 140 acquisition, reads maintenance data, and monitors PIC operations along the RS232 line. The line-scan camera communicates
 141 with the PC via Gigabit Ethernet.

142 The instrument is placed outdoor, on the roof of the "Physique" shelter, approximately 6 m above the ground.

143 ICE-CAMERA was first installed in Concordia in 2012, but replaced in 2014 with its improved version, described here.

144 From then on, the instrument works year-round to produce precipitation data, every hour. Standard meteorological data are
 145 automatically obtained from local weather station AWS MILOS 520.

146

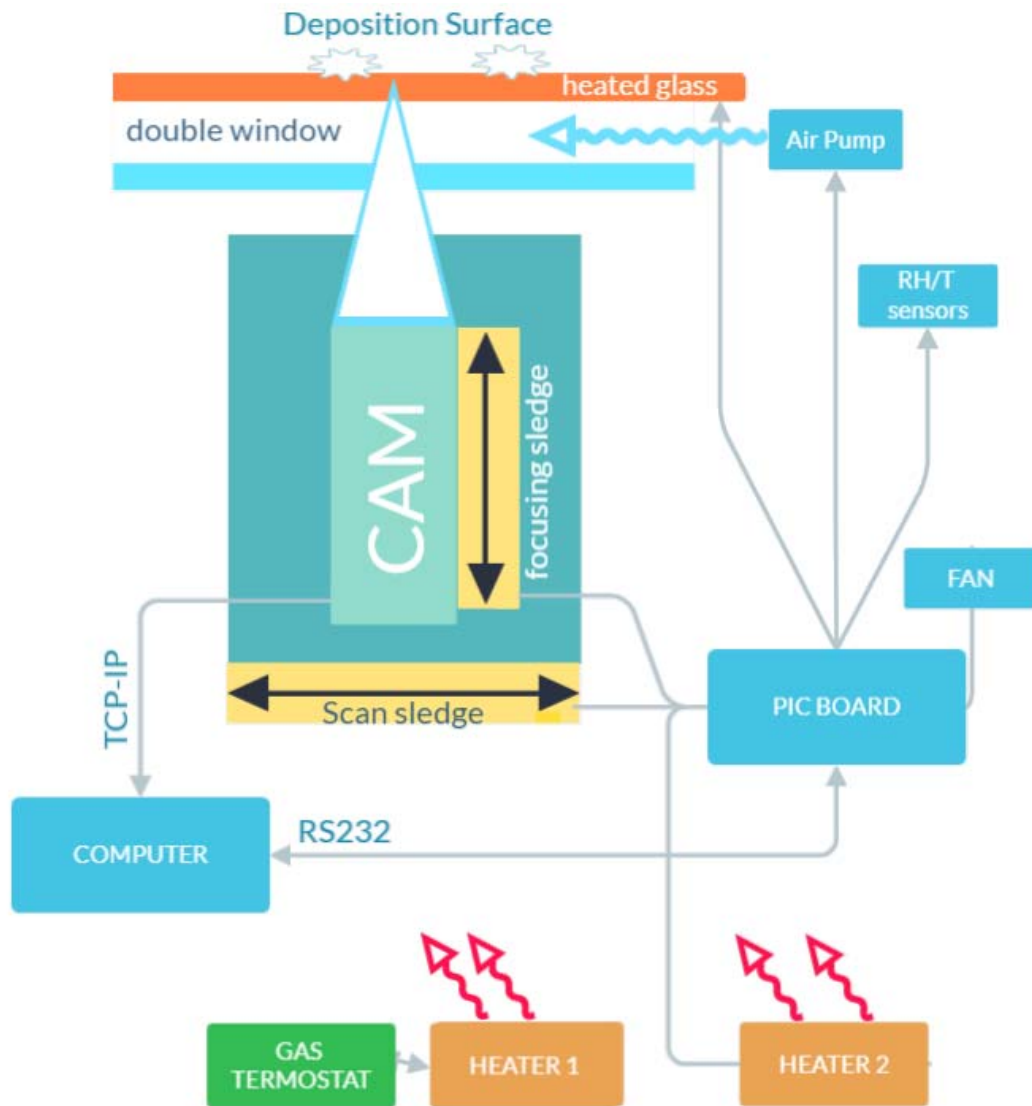


Fig. 3: Basic schematics of the instrument

148

149

150

151

152

153

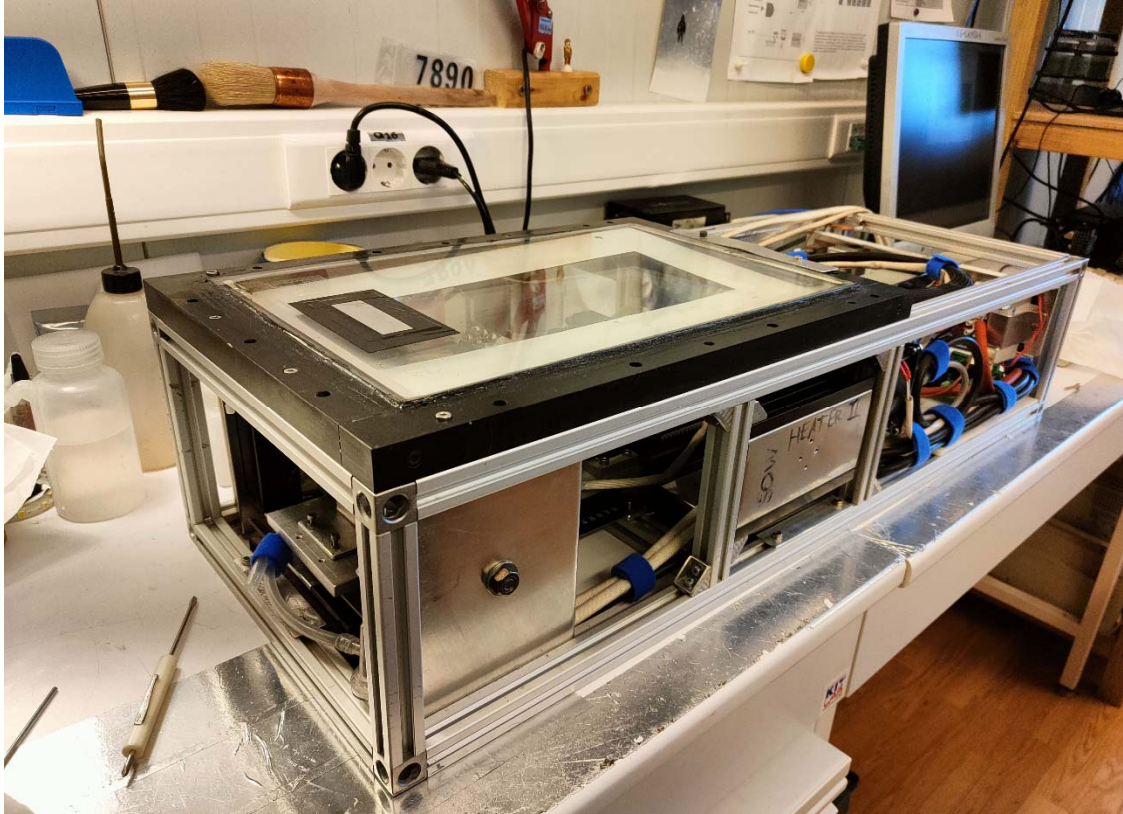
154 2.2 The line scan Camera.

155 1) A linear scanning GigE Vision monochrome camera (Schafter-Kirchoff SK7500VTF-XB (52.5 mm sensor, 7500
 156 pixels, $7 \times 7 \mu\text{m}$ pixels, 8.2kHz line frequency), equipped with a 1:1 macro lens (APO-Rodagon D1X, f5.6) is used for
 157 the acquisition. The optics were designed by Schafter-Kirchoff in order to have a resolution equivalent to the $7 \mu\text{m}$
 158 pixel size. A 90° bending aluminium mirror is used to look upward. The illumination is ensured by 850 nm LEDs. A
 159 colour filter (Schott RG715, 800-1000 nm band-pass) was used on the CAM lens, in order to have a fully solar
 160 instrument. The line-scan camera assembly is moved by a motorized sledge at a speed of 8 mm s^{-1} in order to scan a
 161 rectangular surface of $55 \times 200 \text{ mm}$, (Deposition Surface, DS), at the center of the window. The final image is
 162 7500×30000 pixel, 12 bits, monochrome. A fine calibration of the actual pixel size of the DS image was achieved by
 163 scanning a calibrated grid (0.1 mm spacing) placed on the DS.

164

165 **2.3 The Focusing.**

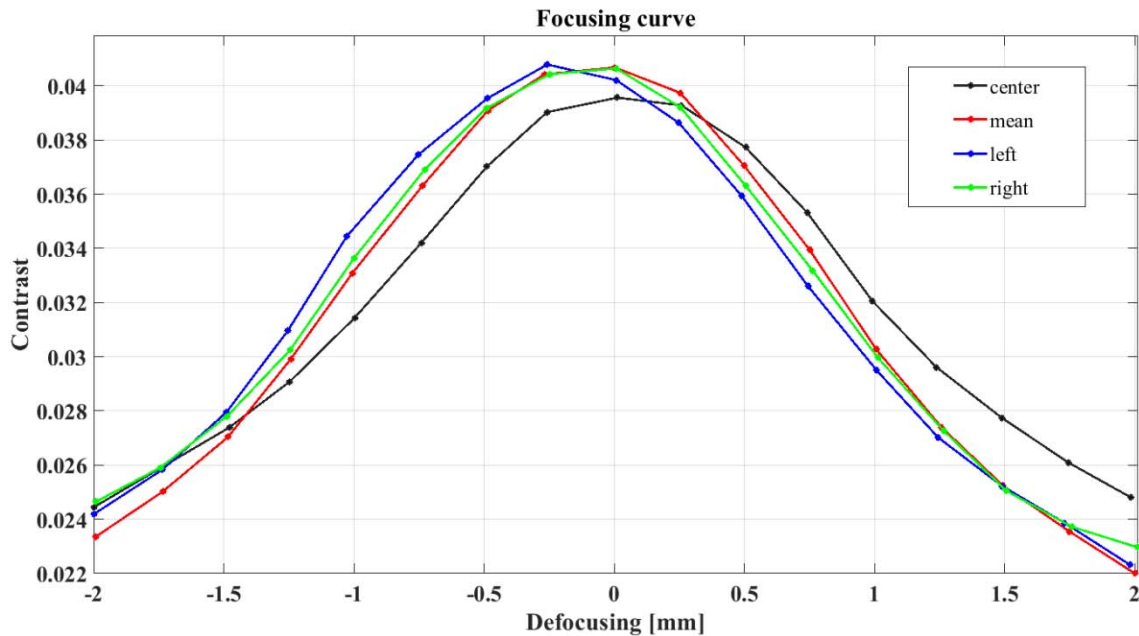
166 In working conditions, the focal depth is ± 0.5 mm. A preliminary and accurate alignment of the motorized sledge plane to
167 the DS ensures uniformity of focus across the DS at room temperature. A motorized focusing sledge, moving the bending
168 mirror, allows to adjust the focus in operating conditions (Fig. 2). As ICE-CAMERA works outdoor at DC, it can
169 experience a broad internal temperature range, from $+5^{\circ}\text{C}$ in summer to -45°C in winter, with quite large temperature
170 gradients across the structure. Thermal expansion and changes in optical refractive indexes result in unpredictable changes in
171 the focal plane. The correction of the focus is thus automatically performed, every 6 hours, by bringing the measuring sledge
172 outside the DS, where a focusing spot (a sandpaper strip) is glued to the window (Fig. 4).



173
174 **Fig. 4: ICE-CAMERA out-of-the-box. The focus target is fixed onto the DS window**

175
176 The porous structure of the sandpaper has a length-scale of the order of 0.1 mm, comparable with the size of the measured
177 ice particles. While calibrating, the focusing sledge is moved by ± 2 mm around the actual position in 0.25 mm steps.
178 Successive images of the sandpaper are taken and their contrast (defined as the standard deviation of the intensity of the
179 pixels) is measured. After a Gaussian-fit of the contrast as a function of defocusing (Fig. 5), the position corresponding to
180 the maximum contrast is obtained, and the mirror sledge is moved into that position. **The typical focal spot adjustment**
181 **between two consecutive calibrations is 0-0.25 mm. The calibration takes approximately 5 minutes. For this reason, it is not**
182 **done after each measurement, so as to save PC resources for data processing.**

183



184

185

186 **Fig. 5: Typical focus calibration: Contrast is calculated in three sectors of the image: center, left and right. The contrast**
 187 **throughout the image is also displayed (red). The slight difference in focus (0.2mm) between the center of the image and the side**
 188 **wings is a normal lens effect.**

189

190 **2.4 Illumination.**

191 Lighting is supplied by two 850 nm LED (TSHG6200) strips. Both arrays illuminate the scan line symmetrically and
 192 approximately 45° from the optic axis in order to minimize multiple reflections in the double window and within the camera
 193 lens. Infrared illumination was chosen in order to work in solar-blind conditions. This is particularly important, as the linear
 194 scanning camera always looks upward, to the sky. The uniformity of lighting along the linear CCD image was tested by taking
 195 an image of the same sandpaper used in the focus. The intensity profile along the CCD image was measured, and the intensity
 196 of the LEDs eventually changed to have a final intensity uniformity across the entire frame of less than 15%.

197

198 **2.5 The Deposition Surface (DS).**

199 The DS is a 10 mm thick, electrically-heated glass (E-GLAS, Saint-Gobain). This glass is transparent at 850 nm, and is
 200 electrically heated with 45 V ac, 1000 Wm⁻² when sublimating the ice particles. A second, 2 mm thick, optically graded glass
 201 sheet (an ordinary flatbed scanner optical glass), placed 13 mm under the DS, makes up with the DS a double window. This
 202 arrangement is necessary in order to keep the DS thermally insulated from the heated, interior of the instrument. A
 203 thermocouple is attached to the DS, while other thermocouples monitor window inter-space temperatures. A DS temperature
 204 of (at least) 3 °C above air temperature is enough to prevent the formation of frost on it in any season, as suggested by
 205 Tremblin et al., (2011) (Fig. 6).



Fig. 6: ICECAMERA at -70°C , Concordia station winter: the DS is free of frost

207

208

209

210

211 During the sublimation period (Sect.2.7), ambient air is pumped for five minutes by means of a 3.5 l/m miniature pump
 212 through the double window space, in order to keep the internal surfaces of the double window always free of frost. Using
 213 inert gases such as argon in the double window space for the same purpose proved unsuccessful in Concordia at the
 214 extremely low winter temperatures. In order to avoid the eventual accumulation of wind-drifted snow, the DS has no walls or
 215 obstacles all around. Furthermore, the instrument is located on the roof of a shelter, almost 6 meters above the ground, an
 216 altitude where blowing snow is not normally important at Concordia. Libois et al. (2014) identify drifting snow events at
 217 Dome C when the 10-m wind speed exceeds 7 m s^{-1} . Assuming a logarithmic wind speed profile between the surface and
 218 10-m and an aerodynamic roughness length value of 1 mm (Vignon et al., 2016), this corresponds to a wind speed threshold
 219 value of 5 m s^{-1} at 6 m above the ground. Winds below this threshold (near the annual average wind speed in DC) are not
 220 expected to carry blowing snow to the DS. In addition, blowing snow impacts the flat horizontal and smooth DS at very
 221 small angles, with a very limited chance of sticking to it. As a consequence, ice particles collected on the SD can be
 222 considered representative of precipitation. Since DS is warmer than air, there is no secondary growth in deposited ice.
 223 Instead, the partial sublimation of ice particles before scanning could not be excluded, especially in summer. This topic
 224 needs additional field work and will be modelled in Sect. 3.2.

225

226 2.6 The thermal control.

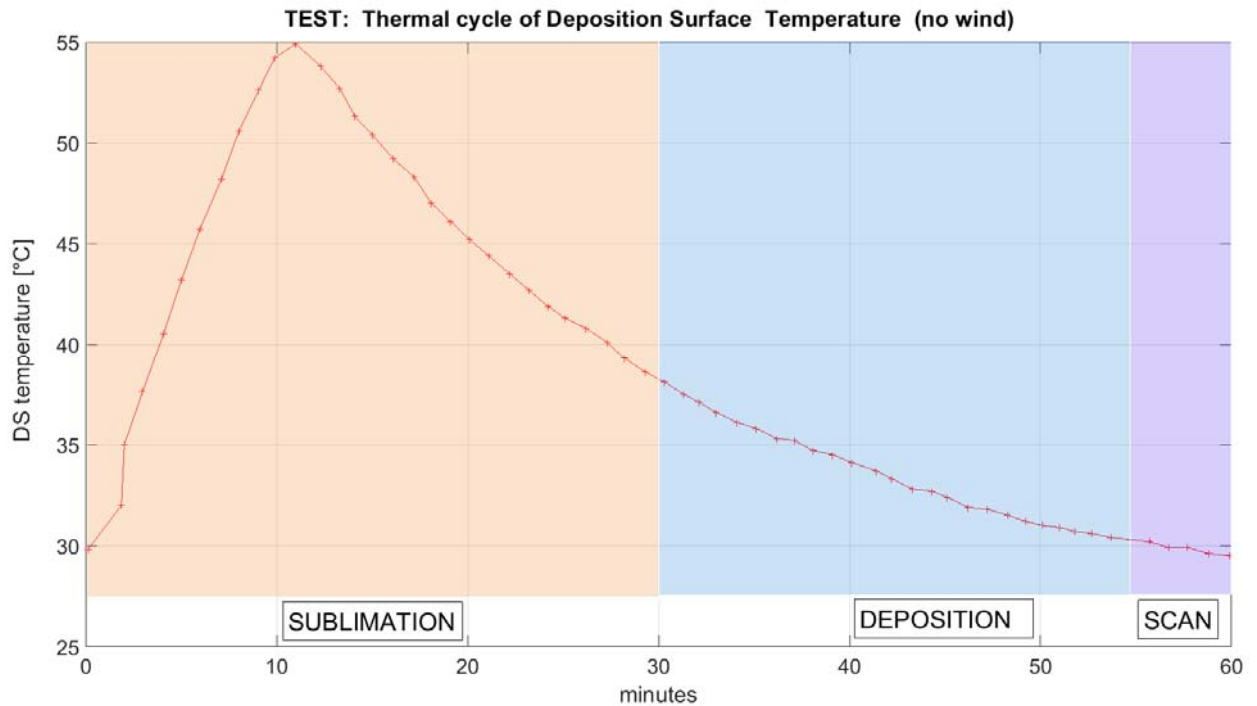
227 The temperatures measured by the ICE-CAMERA sensors are continuously transferred to the computer. The NI-Labview
 228 software controls the internal temperature of ICE-CAMERA above -40°C , and the DS temperature always under -5°C ("Heater
 229 2" in Fig. 3). These conditions are maintained throughout the year during every phase of the measuring cycle. An independent
 230 wired thermostatic system ensures backup temperature control in the event of a PC or PIC board failure ("Heater 1" in Fig. 3).
 231 After a black-out, when the power is restored, a timer is used to heat the inside of the instrument before turning on the
 232 electronics. This is important at Concordia to prevent damage to standard electronics with typical operating temperatures of
 233 40°C .

234 In winter, a 40 mm thick Styrofoam coat is added around the instrument for increasing thermal insulation, whereas in summer,
 235 a Mylar sunscreen prevents overheating of the DS above -5°C in the hot days (Fig. 1). In warm weather, outdoor air is carried

236 inside the box with a tangential fan, for better cooling of the instrument.
237

238 2.7 Sublimation-deposition cycle.

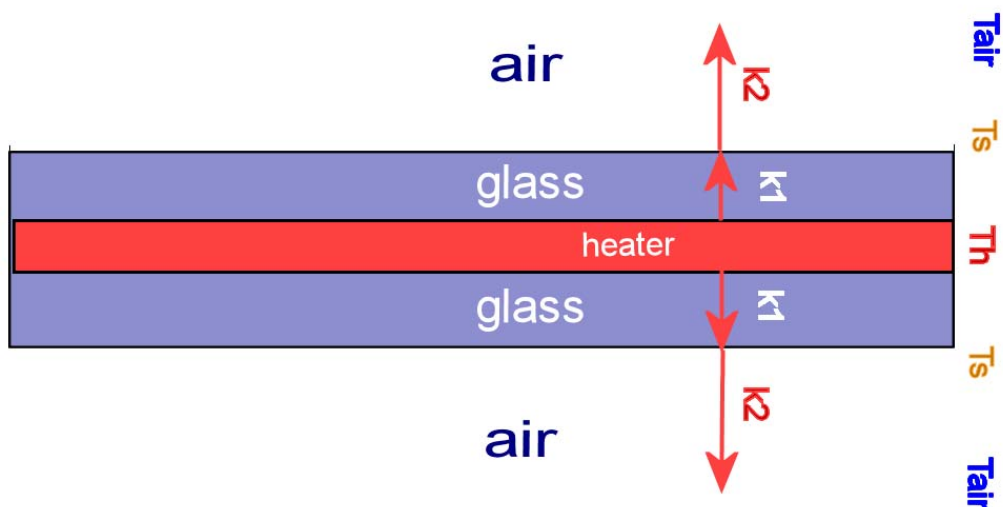
239 After an entire scan of the DS, electricity is applied to the window to sublimate the particles. The heating rate of the DS
240 depends primarily on the thermal constants of the heated window, and secondarily on the wind speed. An indoor test (Fig.
241 7), showed a heating of rate of $2.5^{\circ}\text{C min}^{-1}$, and a cooling rate of $1^{\circ}\text{C min}^{-1}$.
242



243 Fig. 7 : Indoor test of DS heating-cooling rates within a 60 min cycle. Sublimation, Deposition and scan periods are shown
244

245 The cooling rate is almost 50% of the heating rate just due to the sandwich-like structure of the heating-glass, with the
246 heating layer at the middle (Fig. 8).

247



248 Fig. 8: The thermal structure of the electrically-heated glass
249

250 The conductive heat transfer coefficient of the glass ($k_1=0.8 \text{ W m}^{-1} \text{ K}^{-1}$) is much greater than that of the air ($k_2=0.025 \text{ W}$
251 $\text{m}^{-1} \text{ K}^{-1}$). During glass heating, heat is transferred rapidly (with thermal constant k_1) to the DS from the electrically-heated
252 inner layer, while during cooling the heat transfers from the DS to the air occurs slowly (with a thermal constant closer to
253 k_2).

254 Outdoor tests carried out in summer at DC (-30°C air temperature) showed a heating rate of $3 \text{ }^\circ\text{C min}^{-1}$ in still air, $2.5 \text{ }^\circ\text{C}$
255 min^{-1} with 2.5 m s^{-1} wind speed, and $1.8 \text{ }^\circ\text{C min}^{-1}$ with 5 m s^{-1} wind speed. In all cases, the cooling rate was approximately
256 $1.5 \text{ }^\circ\text{C min}^{-1}$.

257 An outdoor sublimation test (-30°C air temperature, wind speed $<3 \text{ m s}^{-1}$) performed with snow manually spread on the DS
258 showed that, after applying heating for 10 minutes (up to a DS temperature of -8°C) the sublimation of the majority of
259 particles (diameter $<1000 \text{ }\mu\text{m}$) was complete within 20 minutes after turning off the heating, with just a few big grains (initial
260 diameter $>1000 \text{ }\mu\text{m}$) still present after 30 minutes.

261 After these tests, the glass heating period was set at 10 minutes (the heating is stopped anyway if the DS temperature exceeds
262 -5°C to avoid melting of the ice in summer). At the peak of the sublimation period, DS resulted warmer than air of about dT
263 $= 20^\circ\text{C}$. Once the heater is turned off, and after a cooling time of 20 minutes, the DS temperature comes back warmer than
264 the air by about $dT = 5^\circ\text{C}$. The "sublimation period" is considered complete, and ice particles accumulate again on the DS,
265 with no relevant sublimation ("deposition period" in Fig. 7). At the end of the deposition period, a scan of the DS is carried
266 out, for a duration of one minute. If no ice particles were detected on the previous scan, the DS heater is not applied,
267 sublimation is not needed. The effective deposition period depends on the temperature, wind and exposure to the sun in
268 summer. This uncertainty, combined with occasional wind removal and particulate sublimation (Sect. 3.2) during the
269 deposition period, prevents the use of ICE-CAMERA for rigorous quantitative precipitation studies.

270 DS surface temperature is actually measured by using a small thermocouple. This measurement implies great uncertainties due
271 to the radiant warming of the sensor in summer and the difficult thermal coupling with the glass surface. The non-contact
272 measurement of DS temperature by means of IR sensors would also be ineffective in winter conditions.

273

274 **3.1 Adhesion of ice particles on the DS.**

275 The adhesion of ice crystals to the smooth DS is caused by two principal reasons: Van der Waals and electrostatic forces.
276 Eidevåg et al (2020) studied the adhesion of dry snow particles after 90° impact to different wall materials. They considered
277 models for normal direction, tangential sliding, and tangential rolling that account for the adhesive Van der Waals interaction
278 of spherical ice particles ($25\text{-}275 \text{ }\mu\text{m}$ diameter) and their aggregates. The Johnson-Kendall-Roberts (JKR) model for adhesion
279 was used. Their findings showed that the maximum normal velocity at which spherical ice particles adhere to a glass surface
280 decreases with particle diameter. Spherical particles of $100 \text{ }\mu\text{m}$ would adhere for speeds less than 0.02 m s^{-1} . In the case of
281 agglomerates with a diameter of $315 \text{ }\mu\text{m}$, composed of 1000 spherical ice particles $25 \text{ }\mu\text{m}$ diameter each, the sticking velocity
282 for the adhesion of 90% agglomerates normally hitting the surface increased to 0.5 m s^{-1} , just one third of the Stokes
283 sedimentation speed (1.7 m s^{-1}) calculated for the same aggregate at DC conditions ($T_{\text{air}}=-50^\circ\text{C}$, air density $=1.03 \text{ kg m}^{-3}$,
284 dynamic viscosity $= 1.44\text{E-}5 \text{ Pa s}$). These results show that the $300 \text{ }\mu\text{m}$ diameter ice particles could stick to the ICE-CAMERA
285 window for Van der Waals' forces alone. Ryzhkin and Petrenko (1997) showed that static charges, naturally transported by
286 ice crystals, increase adhesion. The electrostatic interaction between the ice and the surface is significantly stronger than the
287 van der Waals forces at distances greater than the inter-molecular forces. This effect explains the attachment of the largest ice
288 crystal to the DS of ICE-CAMERA. Once attached to the DS, the weak winds generally observed at DC cannot detach the
289 particles from the DS. Particulates are protected by the boundary layer (BL) that forms on the DS. The 99% thickness of the
290 laminar BL (Blasius solution) at the centre of the DS (0.15 m distance from the window edge) is expected to be 7 mm at -50°C
291 with a wind speed of 1 m/s , decreasing to 2 mm at 10 m/s wind speed. As a result, the particles deposited on the DS are
292 protected against the wind.

293

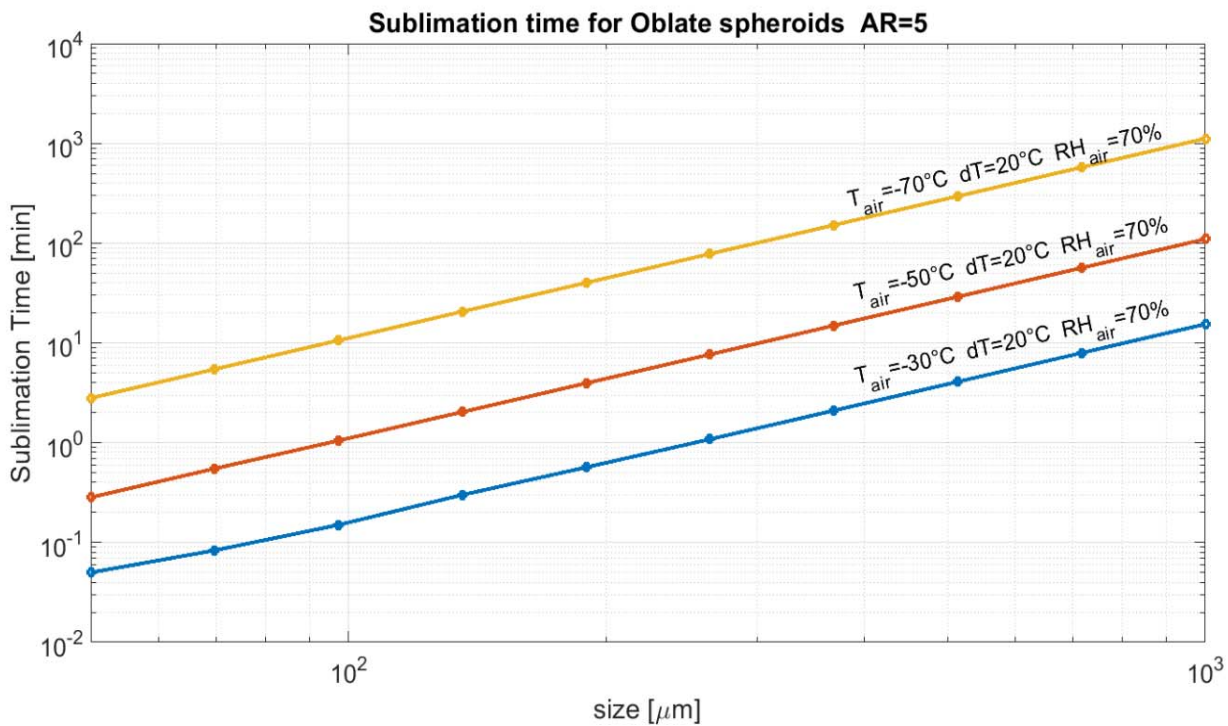
294

295 3.2 Sublimation of ice particles.

296 The DS of ICE-CAMERA is always warmer than the surrounding air. This is necessary to eliminate hoar, enabling the device
297 to be used in all DC conditions. The adverse effect is an accelerated natural sublimation of deposited particles. A wide range
298 of experimental and theoretical research efforts has characterized the effects of temperature and super-saturation on ice crystal
299 growth rates and morphology under conditions relevant to atmospheric processes (for example Lamb and Hobbs, 1971;
300 Libbrecht, 2005; Libbrecht, 2017). The wide variety of ice crystals found in nature has sparked an interest. Sublimation was
301 sometimes regarded either as the opposite process, or a less intriguing process, and was less visited in lab studies.
302 Nelson,(1988) sublimated numerous, 100 μm diameter plate crystals ($0.1^\circ\text{C} > T > -18^\circ\text{C}$, 0.05% to 5% sub-saturation) showing
303 that the crystals first lost sharp edges, and finally evolved into spheroidal particles, and the aspect ratio remained almost
304 constant. The sublimation rates were accurately predicted by the diffusion equation with the surface vapour density at the
305 equilibrium value for a uniform surface temperature. The sublimating crystal reaches a self-preserving shape that is one of the
306 shape preserving solutions of the diffusion equation. Ham (1959) showed that ellipsoids and thus spheroids preserve shape
307 during growth and sublimation if the grain surface has a uniform temperature. Jambon-Puillet et al.(2018) also showed
308 experimentally and theoretically that sublimation first smooths out regions of sharp curvature, leading to an ellipsoid. The
309 second stage is the sublimation of the self preserved ellipsoid shape. The entire process may be modelled as a vapour diffusion
310 problem, mathematically equivalent to the resolution of the electrical potential around a charged conductor. Using this analogy,
311 they provided a mathematical method for simulating the sublimation of the ice particle. The sublimation of the ellipsoid turned
312 out mathematically simple, and their method was adopted in this work to numerically simulate the second stage of sublimation
313 of ICE-CAMERA particles.

314 Monodispersed oblate spheroids with an aspect ratio (AR) of 5, in thermal equilibrium with the DS, were assumed in the
315 simulations as a surrogate for ice plates. The two major spheroid axes coincide with the «diameter» of the oblate spheroid, D.
316 In the model, D, DS temperature, air temperature and relative humidity with respect to ice (RHair) can be changed. The
317 sublimation time required for full sublimation of a spheroidal ice particle was computed. As sublimation accelerates when the
318 particle is going to vanish, the time necessary for the complete sublimation is only slightly larger than the time necessary to
319 reduce the particle to the minimum particle size ($D=60 \mu\text{m}$) accepted by ICE-CAMERA image processing. The simulations
320 assume that the preliminary sublimation of the high-curvature parts of the particle (sharp edges, corners, surface irregularities)
321 was already completed, so that the calculated time of sublimation must be considered as a lower limit for real-world crystals,
322 and probably almost one half of the overall duration of sublimation (Jambon-Puillet et al.,2018). Simulations also assume the
323 thermal equilibrium between the particle and DS, a condition which is not necessarily satisfied on the thermally insulating
324 glass surface of the DS. Figure 9 shows the total sublimation time with the DS heated $dT=+20^\circ\text{C}$ above air temperature
325 (sublimation period). The humidity resulted irrelevant in this case, and only results for 70% RHair are shown. Results show
326 that at -30°C air temperature (summer conditions in DC) complete sublimation can occur within a few minutes after attaining
327 the DS sublimation temperature, for all particle sizes up to 1 mm. At lower air temperatures, the sublimation time increases:
328 at -70°C (winter temperature in DC), particles smaller than 100 μm in diameter still disappear within 10 minutes, while larger
329 particles can survive along the sublimation period. Simulations showed that, at -70°C , dT should be increased to $dT=60^\circ\text{C}$ in
330 order to ensure the complete sublimation of ice particles up to 1 mm diameter during the sublimation period. This is actually
331 not possible with the electric heated window glass adopted, but could probably be achieved by microwave heating.

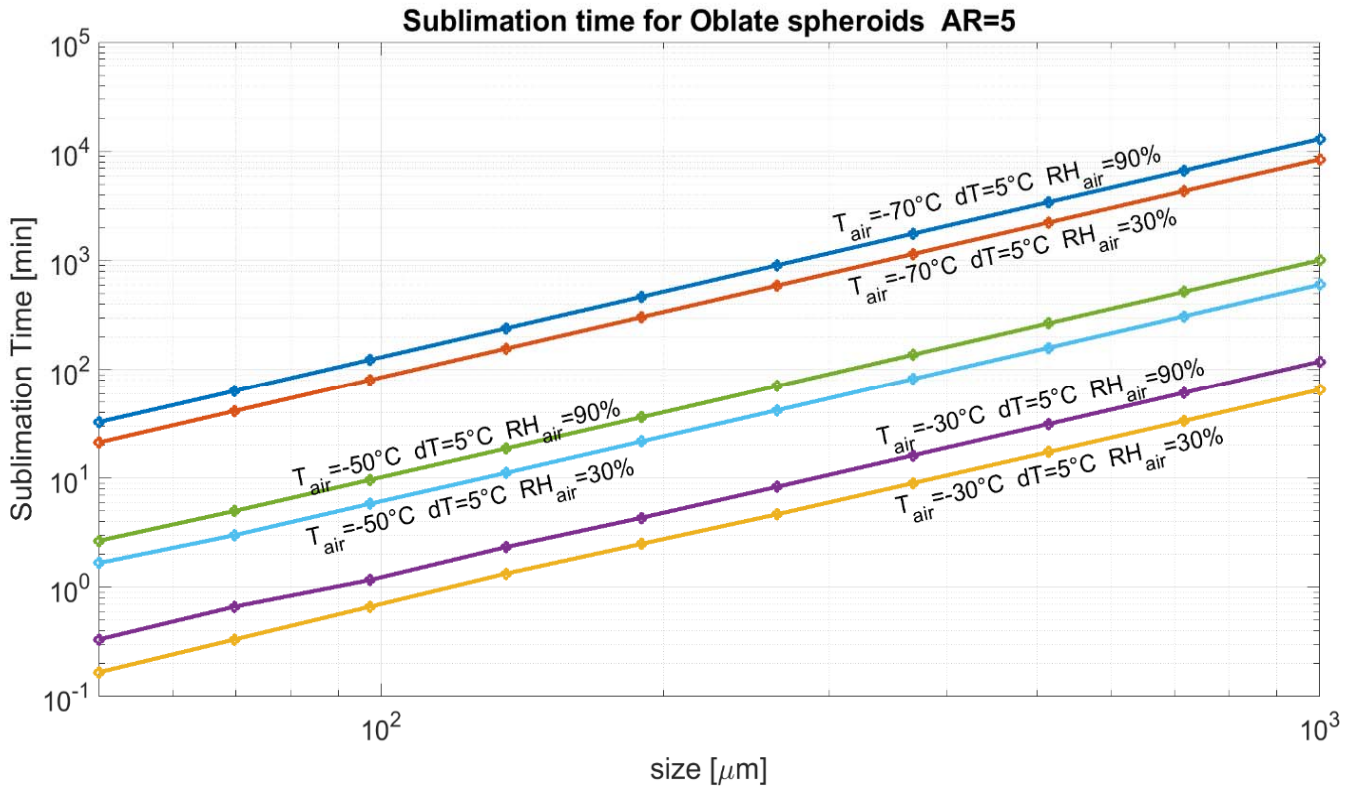
332



333
334
335
336

Fig. 9: Sublimation time of monodisperse oblate spheroids at varying air temperatures, with $dT = 20^\circ\text{C}$ (sublimation period).

337 After the sublimation period, most of the particles previously collected on the SD are sublimated, and a new deposition period
 338 begins. Even during this period, sublimation still acts on ice particles, albeit slowly. Figure 10 shows the sublimation time
 339 expected for monodisperse spheroids during the deposition period. The DS was considered 5°C hotter than air. As shown,
 340 during the deposition period the relative humidity of air also plays a role, even if secondary. In summer ($T_{\text{air}} = -30^\circ\text{C}$),
 341 sublimation can take less than a minute for particles smaller than $100\ \mu\text{m}$ and ten minutes for $300\ \mu\text{m}$ particles. During winter
 342 ($T_{\text{air}} = -70^\circ\text{C}$), all particles are expected to survive through the deposition period. As a rule-of-the-thumb, simulation showed
 343 that working with $dT = +5^\circ\text{C}$ resulted in an increase of the rate of sublimation by a factor 2-3 compared with a DS in thermal
 344 equilibrium with ambient air ($dT = 0$) for the whole range of air temperatures and RH_{air} shown in Fig. 10.
 345 Results of Fig. 10 show that the effective lower limit of ICE-CAMERA particle detection is not limited solely to the resolution
 346 of the optical system and/or image processing software. In summer, particles smaller than $100\ \mu\text{m}$ may be decimated during
 347 deposition, unless they fall just before scanning. Such small particles dominate diamond dust events. As a result, ICE-
 348 CAMERA, during the summer period, is best suited to the study of cloud precipitation. Nevertheless, visual screening of ICE-
 349 CAMERA images showed only a limited number of small particles revealing signs of partial sublimation, such as rounded
 350 corners, smooth edges, or a spheroidal appearance. Some small plates (observed mainly in winter, when sublimation during
 351 the deposition period is very slow) showed smoothed corners, but it is not clear if this was induced by sublimation or is a
 352 natural feature of these ice grains. Also, even in summer, small DD particles such as plates (with no signs of edge smoothing)
 353 were normally observed (Sec. 6.2). It is probable that most particles (other than, probably, pristine plates) never achieve
 354 thermal equilibrium with the DS glass, and that the results of Fig. 10 should be considered as the worst case. Also, the
 355 sublimation of the high-curvature parts of the particle prior to assuming the spheroidal form (Jambon-Puillet et al., 2018) could
 356 take much more time than the sublimation time calculated here for the spheroid. A series of consecutive DS scans at fixed air
 357 temperatures is needed to measure the effective sublimation rate of small particles in deposition conditions ($dT = +5^\circ\text{C}$).



359

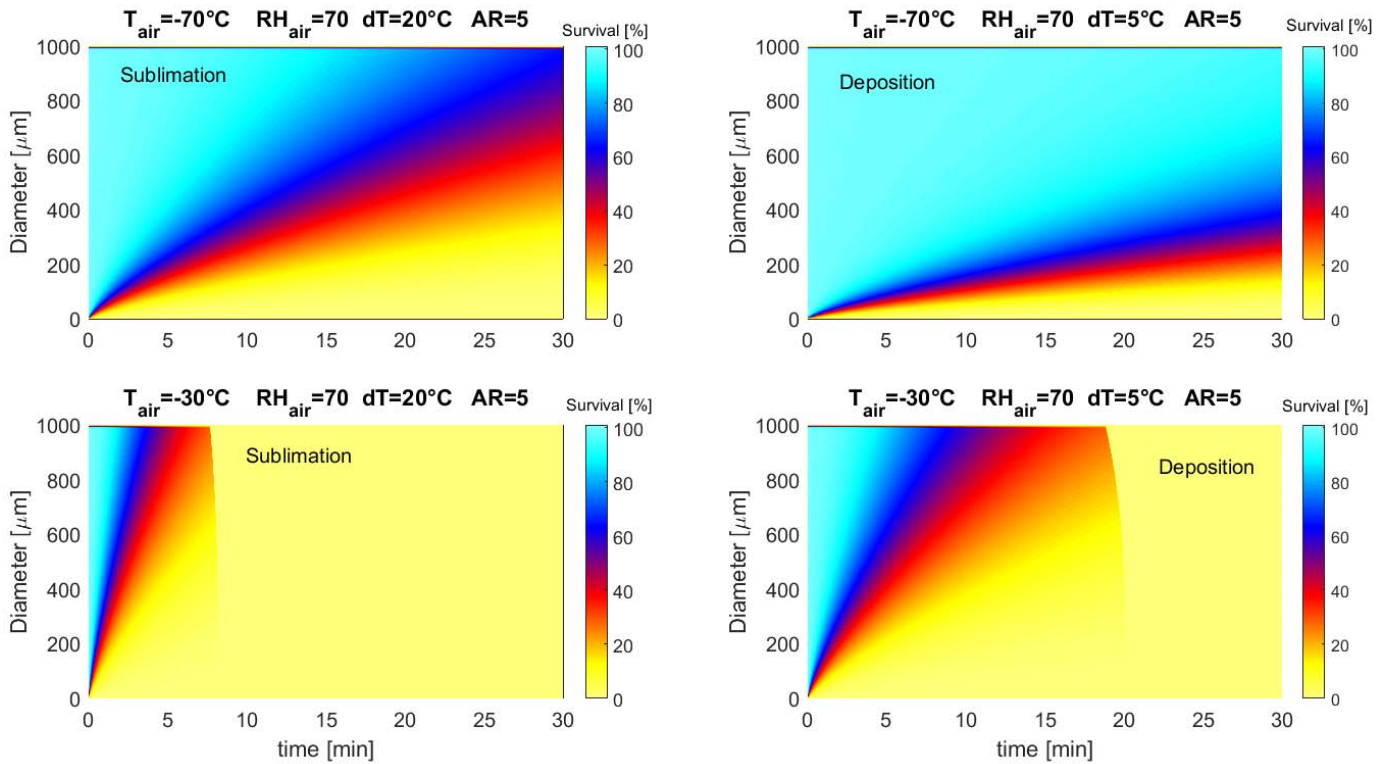
360

361 **Fig. 10: Sublimation time for oblate spheroids at varying temperatures and air humidity, with a DS temperature of**
 362 **5°C above air temperature (deposition period).**

363

364

365 When a polydisperse particle population is deposited on the DS instead of monodisperse particles, a more complicated
 366 sublimation picture arises, because small spheroidal particles, shrinking, are continuously replaced in the size distribution by
 367 sublimating, initially bigger ones. An initial uniform particle size distribution (PSD) of the oblate spheroids (AR=5) was
 368 assumed with diameters between $D=1$ and $2000 \mu\text{m}$ for the simulations. The evolution over time (1 sec resolution) of the PSD
 369 was calculated (Fig. 11) in terms of particle survival (the ratio between the actual number of particles in a certain size bin and
 370 the initial number in the same bin). No vapour competition between ice particles was taken into consideration in the
 371 simulations. Results are similar to those of monodisperse particles (Fig. 9,10), with a slightly longer time of sublimation for
 372 polydisperse particles compared to monodisperse particles of the same size. Results for an air temperature of -70°C confirm
 373 that most particles larger than $500 \mu\text{m}$ survive, throughout the DS sublimation period ($dT = 20^\circ\text{C}$), longer than 30 minutes.
 374 This means that sublimating by heating the window is quite inefficient for large particles in winter. During the deposition
 375 period, at -70°C losses for sublimation are scarce and limited to particles smaller than $200 \mu\text{m}$. Consequently, double counting
 376 of the same particle ($D > 500 \mu\text{m}$) is possible in two consecutive ICE-CAMERA scans in the cold DC winter. At -30°C air
 377 temperature (summer) the heating of the DS with $dT=20^\circ\text{C}$ leads to the sublimation of most particles up to 2 mm diameter
 378 within 5 minutes. On the other side, during the deposition period particles smaller than $500 \mu\text{m}$ can undergo sublimation over
 379 a period of just 10 minutes in summer, thus limiting the effective period of deposition before a scan. As with monodisperse
 380 particles, this introduces bias in the summer because many small particles (typical of DD) can be removed before they are
 381 measured.

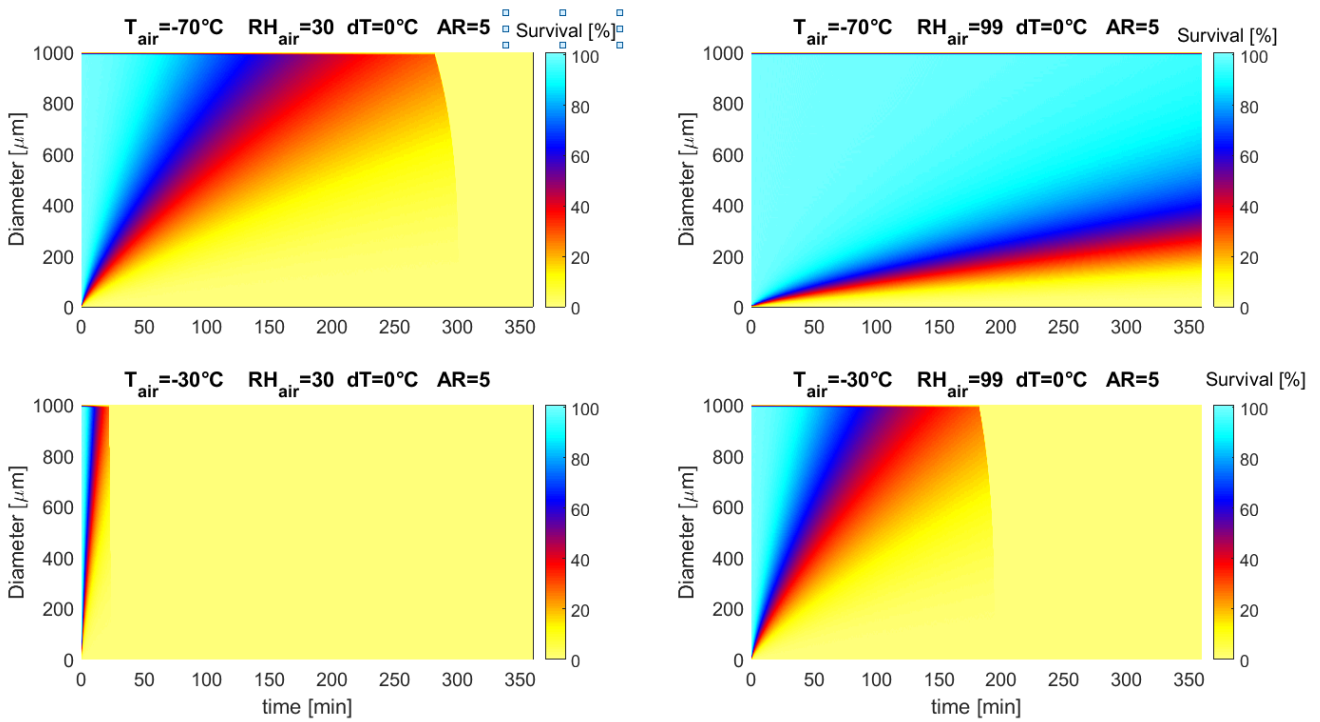


382

383 **Fig.11: Evolution of a originally uniform PSD of ice spheroids ($D=0-2000 \mu\text{m}$, $AR=5$) under different atmospheric**
 384 **conditions. (RH_{air} is a secondary factor affecting the results, shown here for $RH=70\%$).**
 385 **Left: sublimation period; right: deposition period. Top: winter, bottom: summer**

386

387 Even if these results could be disappointing for interpreting ICE-CAMERA data, the same problems affect the actual method
 388 of observing precipitation in DC: Collecting and observing (every 24 hours) the ice particles deposited on flat surfaces
 389 ('benches') is affected by the same problem as collecting particles on the ICE-CAMERA DS with $dT=0$. Fluctuations in
 390 relative humidity over 24 hours result in sublimation and regrowth of particles on the "benches" in an almost unpredictable
 391 manner. Fig. 12 shows the expected sublimation time for particles (with the same PSD of Fig. 11) placed on 'benches' (or
 392 ICE-CAMERA DS) in equilibrium with air ($dT=0$) for extreme, sub-saturated conditions: winter $T_{\text{air}}=-70^\circ$ ($RH_{\text{air}}=30\%$ and
 393 99%), and summer $T_{\text{air}}=-30$ ($RH_{\text{air}}=30\%$ and 99%). The PSD evolution is computed with a resolution of 1 sec for a total
 394 period of 6 hours. The results show that sublimation also works in winter and with almost saturated air ($99\% RH_{\text{air}}$), leading
 395 to a complete loss of small particles ($D < 200 \mu\text{m}$) in a few hours. In summer conditions and $30\% RH_{\text{air}}$ sublimation happens
 396 much more quickly, with the disappearance of all particles up to $2000 \mu\text{m}$ in 30 minutes. With $RH_{\text{air}}=99\%$, sublimation
 397 removes all particles in just a few hours in summer. In presence of wind and dry air, sublimation rate could even increase, as
 398 observed by Grazioli et al., 2017 in coastal areas. These simulations all refer to sub-saturated conditions: in the case of a
 399 'bench' in thermal equilibrium with super-saturated air, hoar form on the surface, with a possible confusion with precipitation.



400

401 **Fig.12: Evolution of a originally uniform PSD of ice spheroids ($D=0-2000 \mu\text{m}$, $AR=5$) under different atmospheric**
 402 **conditions. The DS (or ‘bench’) is in thermal equilibrium with air ($dT=0$). Top: winter, bottom: summer**

403

404

405

406

407

408 **4.1. Image processing.**

409 ICE-CAMERA is not just designed to take photographs of ice particles, but to provide automatic morphometry and
 410 classification of polar precipitation. This was accomplished through the use of image processing and machine learning
 411 techniques. The process is divided into two parts: segmentation and measuring, and classification of ice crystals.

412

413 **4.1.2 Image Segmentation and Measurement.**

414 After acquisition, the raw ICE-CAMERA scans are segmented, using MATLAB software, to isolate all detected particles. The
 415 process follows the workflow of Fig. 13. Refer to Pratt (2007) for image-processing nomenclature, to Walton, 1948 for Feret
 416 measurement, to Russ and Brent Neal (2017) for the nomenclature of standard shape parameters such as Eccentricity, Euler
 417 Number, circularity, roundness, solidity, compactness, form factor, and number of skeletal branches. The normalized central
 418 moments $f1...f7$ were also computed as described by Hu, (1962).

419 The Aspect Ratio (AR) is defined as Feret’s length/ Feret’s width. The Feret-box surface-equivalent diameter (D_f) is defined
 420 as the diameter of the circle of the same area as the Feret bounding box, while the surface-equivalent diameter (D_s) is
 421 defined as the diameter of the circle having the same area as the segmented ice grain.

422

423

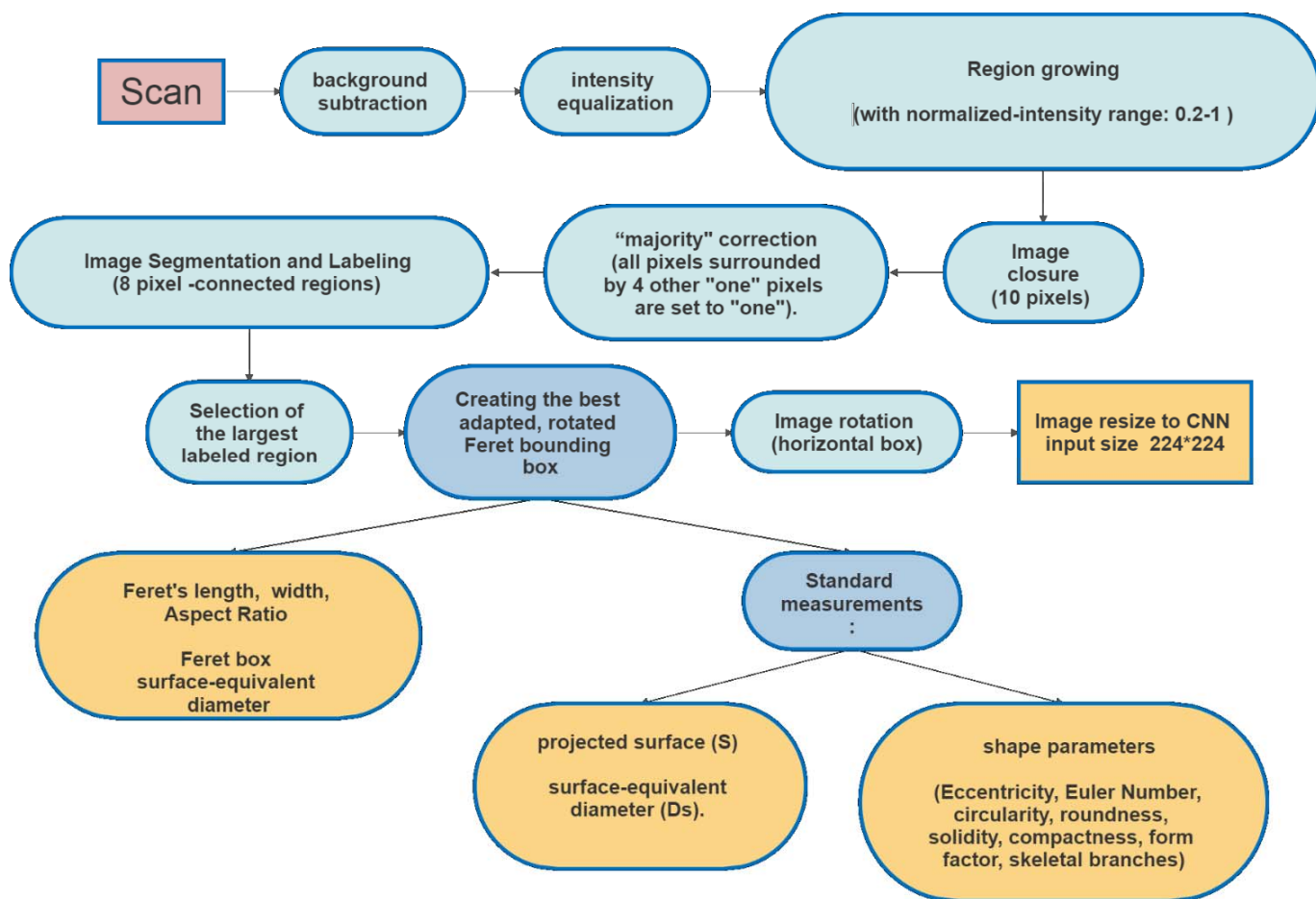


Fig. 13: The image-processing flow chart.

The main steps of Fig. 13 are summarized in Fig. 14 for a rimed, columnar particle

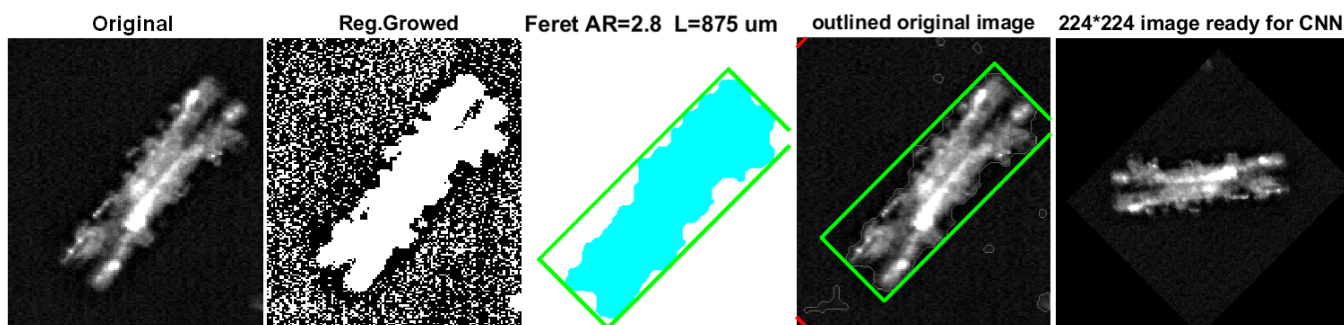
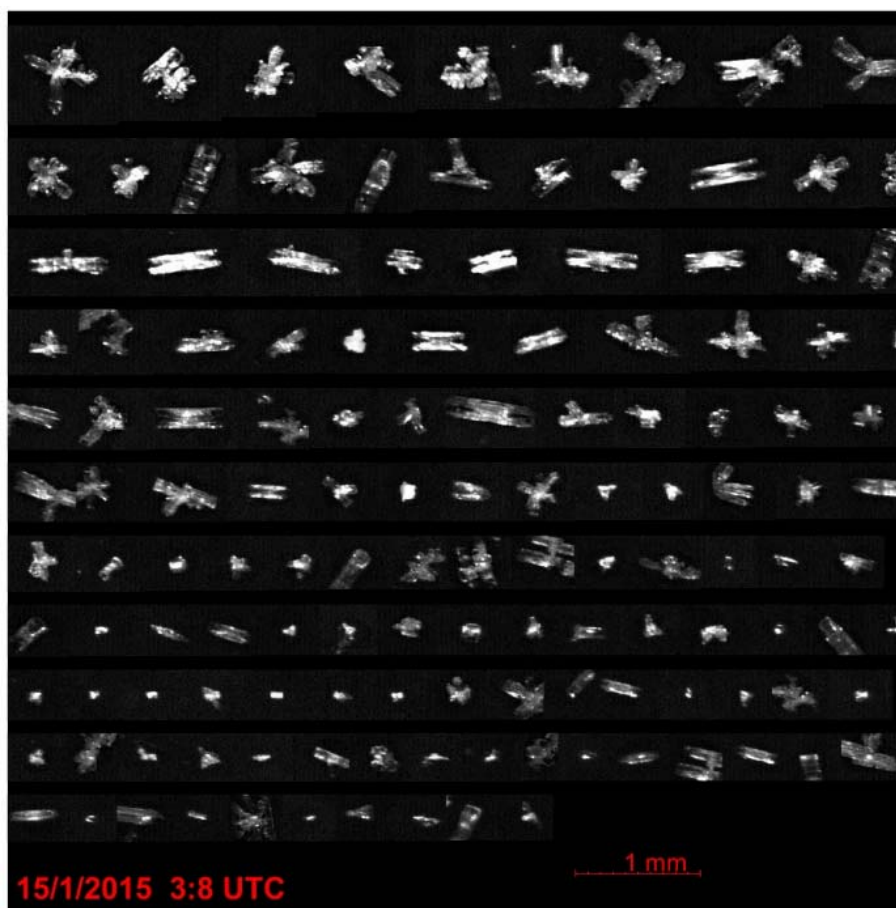


Fig. 14: The original image (in this case a rimed column) is segmented using ‘region-growing’. The projected particle area (clear blue) is calculated. The bounding box is determined (green) and the Feret length and width measured. The image is finally rotated to have the mayor axis horizontal, re-scaled, and resized to the CNN input size.

4.1.3 Summary-image of detected particles.

The bounding boxes of all individual ice particles detected in a scan are sorted by Feret length, and reassembled in a summary-image collecting all segmented particles (Fig 15). Each particle is also associated with a numerical record containing the coordinates of its bounding rectangle on the summary-image, shape parameters, Feret size, time of acquisition and local

441 weather data. In this way, the re-analysis of the summary-image is possible instead of re-processing the original, large image.
442 The original image is ultimately removed.



443
444 **Fig. 15: Example of a summary-image for a single scan.**
445
446

443
444
445
446

447 **4.1.4 Limitations and uncertainties in detecting and sizing ice particles.**

- 448 2) The total number of particles measured is limited to **2000 per scan**, as a result of MATLAB memory limitations.
449 Extra particles are not treated.
- 450 3) Particles below $3600 \mu\text{m}^2$ in bounding-box surface (approximately $D < 60 \mu\text{m}$) are not preprocessed (smaller particles
451 could be detected, but most have a seemingly circular shape due to low pixelation or poor focus).
- 452 4) The segmentation becomes difficult when overlapping particles or aggregates of particles are present. In such
453 situations, double counting of the same particle may occur in up to 12% in a scan in the presence of an intense
454 precipitation event. The same particles can in fact fall inside different segmented areas of the image, because of the
455 lack, on the original image, of defined boundaries between particles. Overlapping particles are normally classed by
456 the CNN algorithm as "clusters". The Feret measurement of these particles is meaningless. At DC this situation
457 occurs only after heavy cloud precipitation, a relatively rare event.
- 458 5) Particles close each other in the original image could be segmented into a single particle by region-growing and thus
459 misclassified.
- 460 6) In the case of defocused images, the particle shapes are all close to a fuzzy, round or elliptical shape, which can cause
461 a misclassification into irregular particles, spheroidal particles or plates. ICE-CAMERA images dominated by this
462 type of particles are normally eliminated during a preliminary manual screening. Also, a few big particles in summer
463 resulted rounded by partial sublimation. A few images containing only rounded or "spheroidal" particles of $500 \mu\text{m}$

464 diameter or greater were collected during the warmest part of summer, and were manually discarded before the
465 statistical data analysis.

466 7) Needles and hexagonal plates (typically small, see Fig.26) may be very bright in ICE-CAMERA images due to
467 enhanced light diffusion at preferred angles. For the same reason, hollow columns sometimes have a shiny spot in the
468 middle. In the case of needles, this effect can reduce the apparent aspect ratio, as the width is apparently increased
469 by the scattered light saturating the camera. For plates, the bright specular reflection blurs sometimes the polygonal
470 contour, especially in the case of small plates.

471

472 **4.2 Automated classification of ice particles.**

473 An initial attempt at automatic classification of ICE-CAMERA segmented images was made in 2014 using shape factors. This
474 kind of technique has also been used by others (e.g. Lindqvist et al., 2012) for attempting the classification of ice particles. In
475 the case of ICE-CAMERA this approach resulted extremely unreliable. A much more promising approach was offered after
476 2015 by the rapid development of transfer learning and convolutional neural networks (CNN) (Le Cun et al., 2015;
477 Schmidhuber, 2014). Xiao et al. (2019) successfully applied deep transfer learning to ice particle images obtained with airborne
478 Cloud Particle Imagers (CPI). The CNN approach has added much value to ICE-CAMERA because a reliable classification
479 of ice particles into simplified classes became possible. The CNN used for the ICE-CAMERA particle classification is
480 "GoogleNet" (Szegedy et al. 2015), a variant of the Inception network, a deep convolutional neuronal network developed by
481 Google scientists. GoogleNet is a type of convolutional neural network based on the Inception architecture. It utilises Inception
482 modules, which allow the network to choose between multiple convolutional filter sizes in each block. The GoogleNet
483 architecture consists of 22 layers (27 layers including pooling layers), and part of these layers are a total of 9 inception modules.
484 In this work, GoogleNet was used in MATLAB R2020b environment. The GoogleNet CNN, pretrained on the ImageNet data
485 set (Deng et al. 2009), was used, with its final, fully connected layer changed to size 14. The input layer of the GoogleNet
486 architecture requires images of size 224 x 224.

487

488 **4.2.1 The CNN classification classes.**

489 Low temperatures and humidity on the high Antarctic plateau reduce the diversity of ice particle shapes. This is observed on
490 the field at DC, at South Pole station (Lawson et al., 2006), and suggested by review works such as Bailey and Hallett (2009).
491 Following an initial survey of the ICE-CAMERA image database, a set of 14 types of particles was selected, as shown in Fig.
492 16. When choosing the 14 classes, I assumed that shapes easily recognizable by a human operator could also be easily
493 recognizable by a CNN. In the following scheme I tried to fit the classes chosen for ICE-CAMERA with the classification
494 scheme of the ice particles of Kikuchi et al. (2013), an updated version of the original classification of Magono and Lee (1966).

495

496

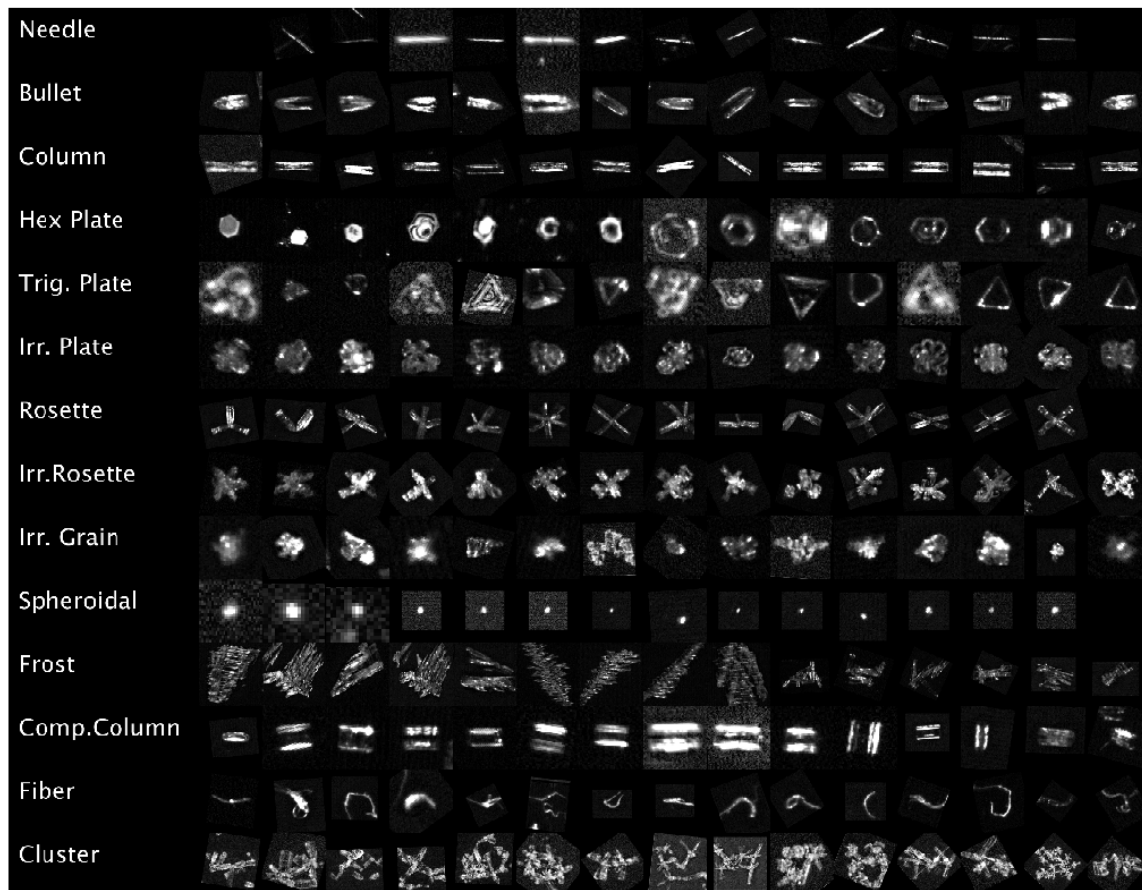


Fig. 16: A sample of ICE-CAMERA images of the 14 classes of ice particles used to train the CNN.

497
498
499

- 500 -**Needles**: covering the classes C1a,C1b,C3d (Kikuchi et al. 2013)
- 501 -**Bullets**: covering the C4b-C4c classes.
- 502 -**Columns**: columns covering classes C2a, R2b, C3a, C3b.
- 503 -**Hexagonal plates**: covering classes P1a, P1b, P1c, P4f, G2a, G3a, CP3f, CP3d.
- 504 -**Trigonal plates**: covering the class G2b.
- 505 -**Irregular plates**: plate-like particles with irregularities, riming, overgrowing plates, etc. But keeping a basic hexagonal
- 506 shape, covering P6a, P6b, P7a, CP6d, R1b, R2b, R2c, R3a, G4b.
- 507 -**Rosettes**: bullet-rosettes or column-rosettes, with a minimum of two branches, covering C2c, C3e, C4d
- 508 -**Irregular rosettes**: rosettes with irregularities, riming, but preserving the typical stellar outline of rosettes. Covering
- 509 classes P7a,P7b,CP2d ,CP4c,CP5a,CP6e,CP6f,CP6g,R1d
- 510 -**Irregular grains**: covering CP3e, CP5a, CP6d, G4c,G4a,I3a,I2a,I1a,H1a,H1b
- 511 -**Spheroidal**: particles with spheroidal or spherical appearance, covering H1a, H1c. (Large particles with $D > 600 \mu\text{m}$)
- 512 detected as 'spheroidal' in DC are usually artifacts caused by defocused images and are not considered in the statistical
- 513 analysis.
- 514 -**Compact columns**: short columns covering classes G1a, C3a
- 515 -**Clusters of particles**: covering A1a, A3a, H2a, H1b, P8b, CP3e, CP5a, CP6h
- 516 -**Frost**: frost formed on the DS plate CP7,CP8,CP9
- 517 -**Fibers**: non-volatile fibrous material (from local human activities, Styrofoam particles, textile particles, dust, etc)
- 518

519 The last two classes are not considered in the statistical analysis of ICE-CAMERA data: they are just used to detect occasional
520 frost formed on the DS, and man-made, non-evaporable (thus persisting on the DS) materials. Uncommon ice particle
521 typologies present at Concordia were not considered in the present work. Trigonal plates have been included, although they
522 are rare, simply because they are seemingly easy to detect with CNN.

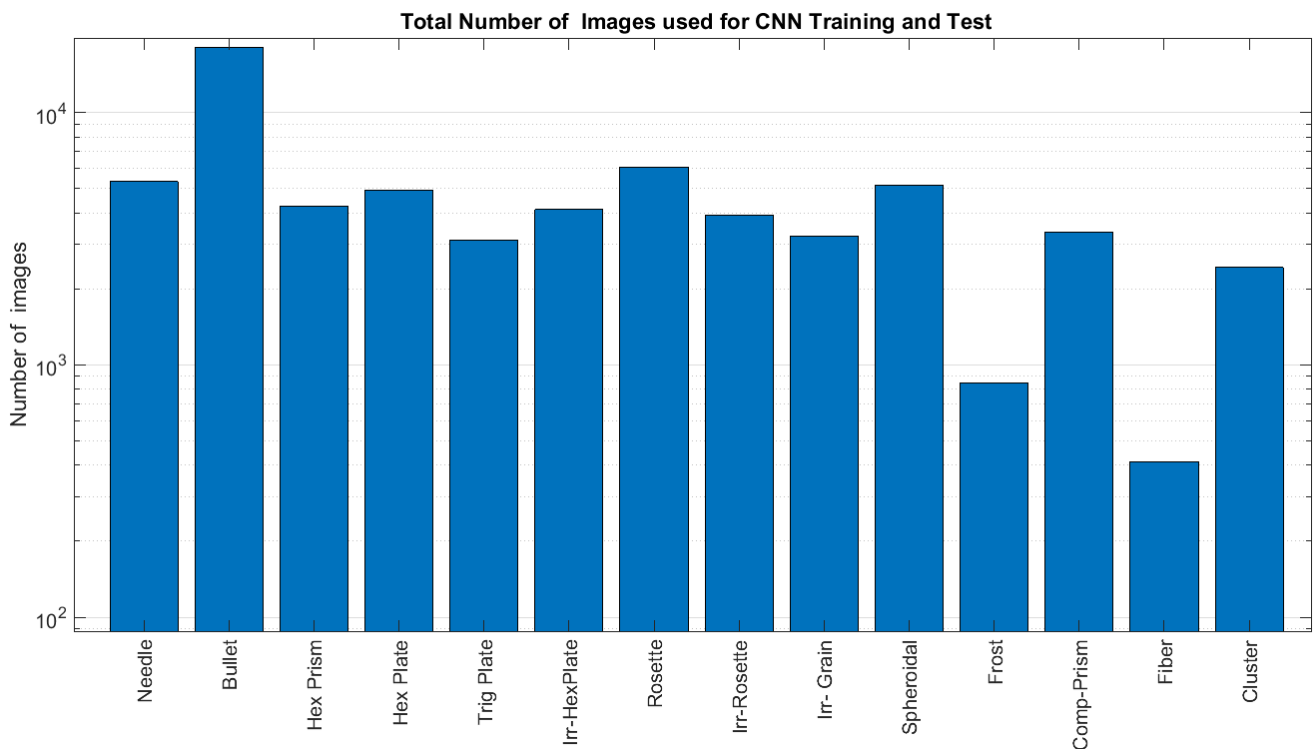
523

524 4.2.3 The training data-set.

525 For the first CNN training, a set of 5500 ICE-CAMERA segmented images of single particles, sampled randomly from the
526 2014-2017 ICE-CAMERA database, have been manually sorted into 14 image data stores, corresponding to the 14 classes.
527 Fourteen of the computer keyboard keys were marked with the symbols of the 14 classes in order to expedite the manual
528 classification of the initial training data set. These images were used for initial CNN training. The resulting CNN was used to
529 classify the ICE-CAMERA data set for the years 2014 to 2017. The classified images were manually cleaned from incorrectly
530 classified images and added to the 14 training image data stores, as new training images, for a second CNN training. This
531 operation was repeated recursively three times in order to broaden the training database and thus increase the accuracy of the
532 CNN classifier.

533 Figure 17 shows the final number of training and test images selected for each class. The total number of images used for the
534 training was 81800. Trigonal plates were rare, and their number in the training dataset was thus artificially augmented by
535 duplicating the training images, in order to avoid their absence in the small (64-images) training mini-batches.

536



537

538 **Fig. 17: The final number of CNN-training + validation + test images**

539

540 4.2.4 CNN training details

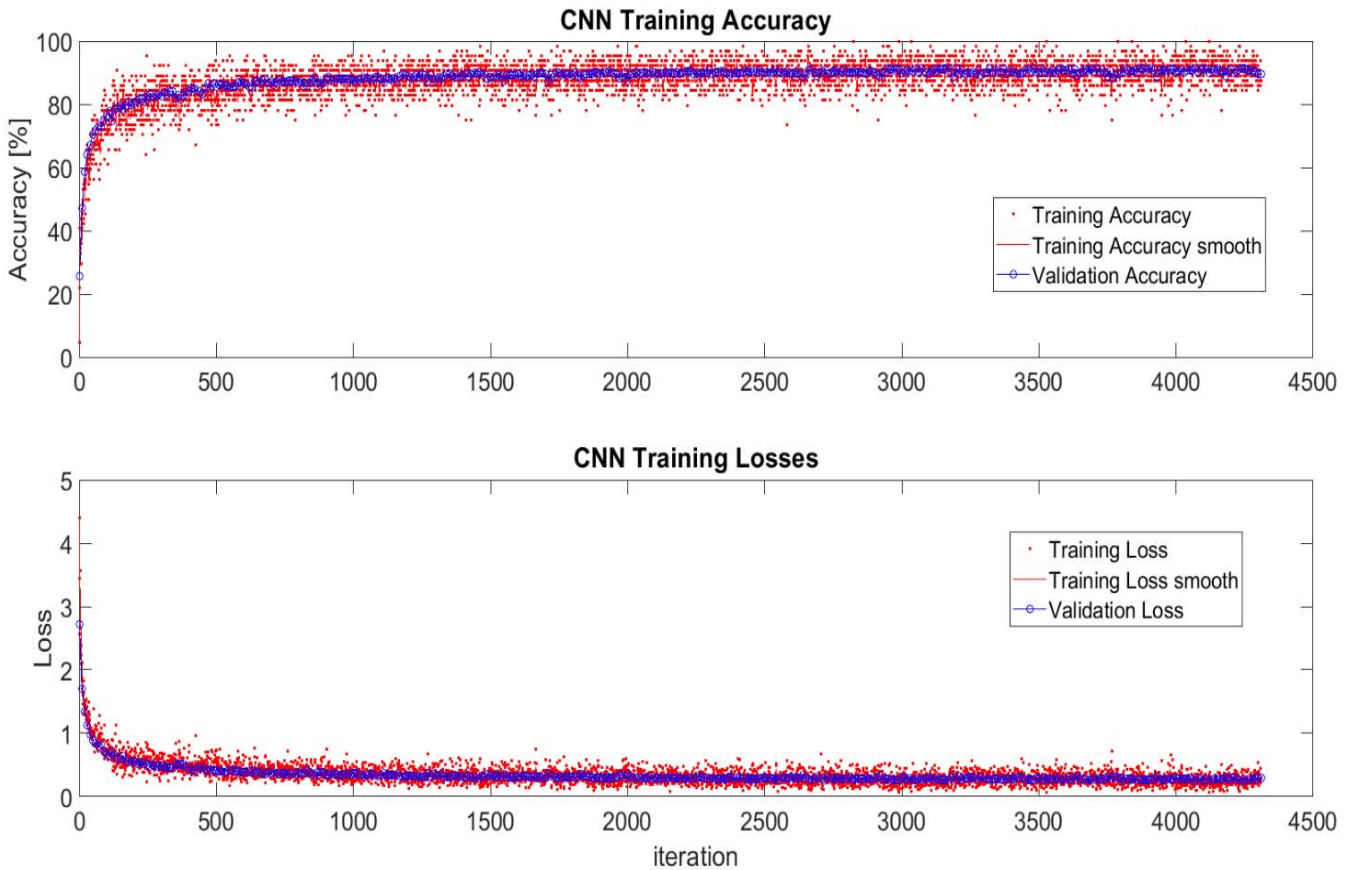
541 To meet Google's input requirements, all images of single particles were resized to 224*224 pixels. In the training process,
542 'data augmentation' was applied to the original data set. Artificially 'augmenting' the image data set has been shown to be
543 effective in CNN training (Shorten and Khoshgoftaar, 2019). Images inside each mini-batch are automatically, randomly
544 'augmented' in order to reduce CNN overfitting. The following transformations were used in augmentation:

- 545 • X, Y reflection
- 546 • random X, Y translations ± 30 pixels
- 547 • Random scaling 80-120%
- 548 Other changes such as rotation have not been introduced since the ICE-CAMERA images to be classified are
- 549 typically oriented horizontally by the image processing procedure (e.g. Fig. 14)

550 The following learning options were utilized in GoogleNet training:

- 551
- 552 Solver: stochastic gradient descent with momentum (SGDM)
- 553 activation: softmax
- 554 Number of Epochs=5
- 555 Learn Rate=0.001
- 556 Batch Size=64
- 557 L2 weight regularization factor=0.005
- 558 Validation frequency= every 30 iterations
- 559 Shuffle of the data set at every epoch

560 10% of the image data set of Fig. 17 was dedicated to validating, 10% for testing, and the remaining 80% of the training. The
 561 evolution of the CNN training in terms of accuracy and losses is presented in Fig. 18. The validation line closely tracks the
 562 training line, showing the absence of overfitting.



563
 564 **Fig. 18: Evolution of the CNN training.**

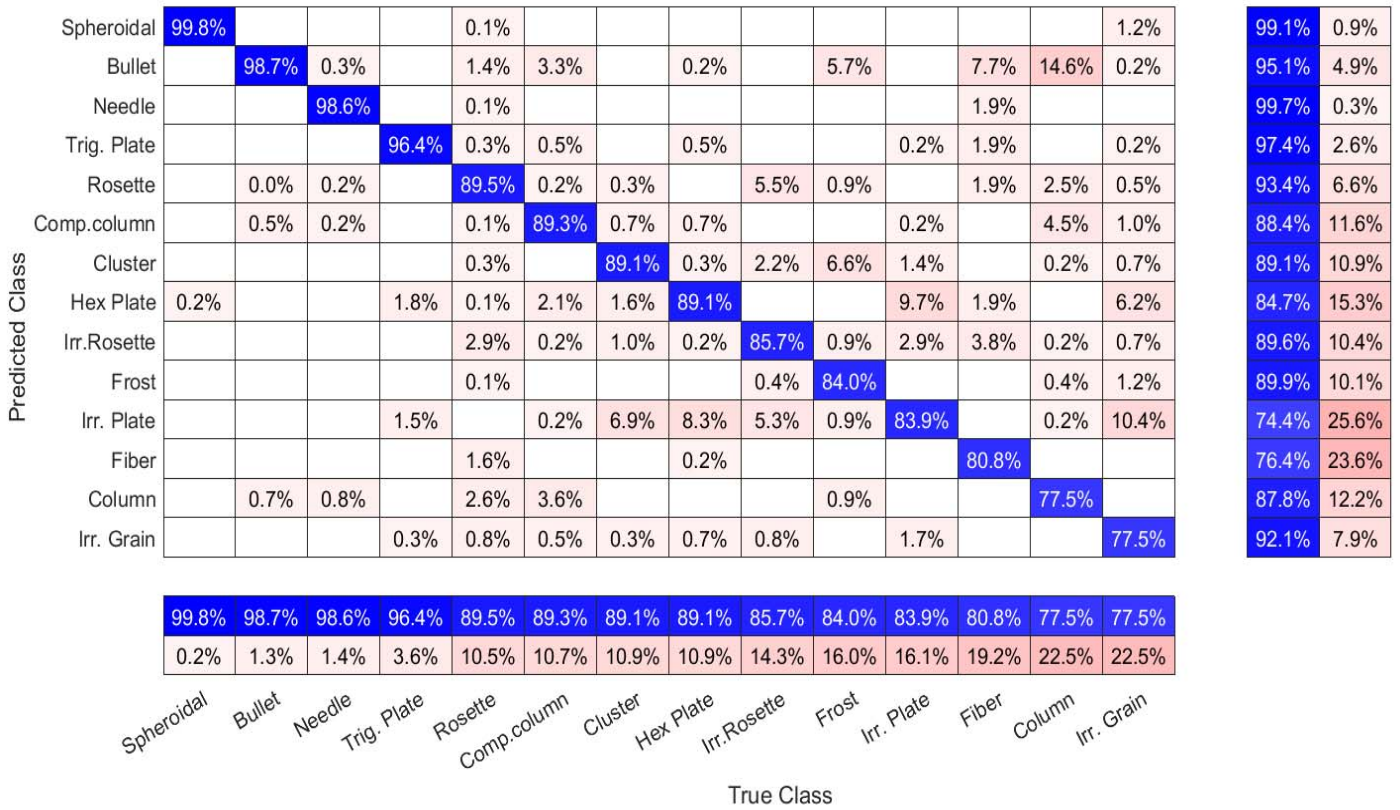
565

566 **4.2.5. Testing the CNN classifier.**

567 CNN's performance test results are summarized in confusing matrix graphs like Fig. 19. Each row corresponds to a
 568 predicted class (Output Class) and each column corresponds to a true class (Target Class). Diagonal cells refer to correctly
 569 classified observations. Off-diagonal cells are improperly classified observations (red color markings increasing
 570 misclassification). The column on the far right of the plot shows the percentages of all the examples predicted to belong to
 571 each class that are correctly and incorrectly classified (positive predictive value and false discovery rates, respectively). The
 572 row at the bottom of the plot shows the percentages of all the examples belonging to each class that are correctly and
 573 incorrectly classified (true positive rate and false negative rate, respectively).

574 **4.2.6 Accuracy of the classifier.**

575 In the column-normalized summary (Fig. 19), the percentages along the i-th column shows the probability (P) of a "true"
 576 particle in class i-th being classified in each of the 14 output classes.



577

578 **Fig. 19: Confusion plot of the CNN (column-normalized)**

579

580 Reading the columns from left to right, the accuracy of the CNN in properly classifying a particle belonging to the i-th true
 581 class (bottom row) can be assessed. The results are summarized below:

582

583 -Good accuracy (P>90%) in identifying needles, spheroidal, bullets, trigonal plates.

584 -Compact columns are misclassified into columns (3% of the time) and bullets (3% of the time).

585 -Hexagonal and irregular plates are confused approximately 10% of the time. This is expected since the edges of the plates
 586 (usually small) are sometimes blurred in the image.

587 -Irregular rosettes are misclassified in 5% of cases as pristine rosettes and in 5% of cases as irregular plates.

588 -Irregular plates are confused with hexagonal plates 10% of times.

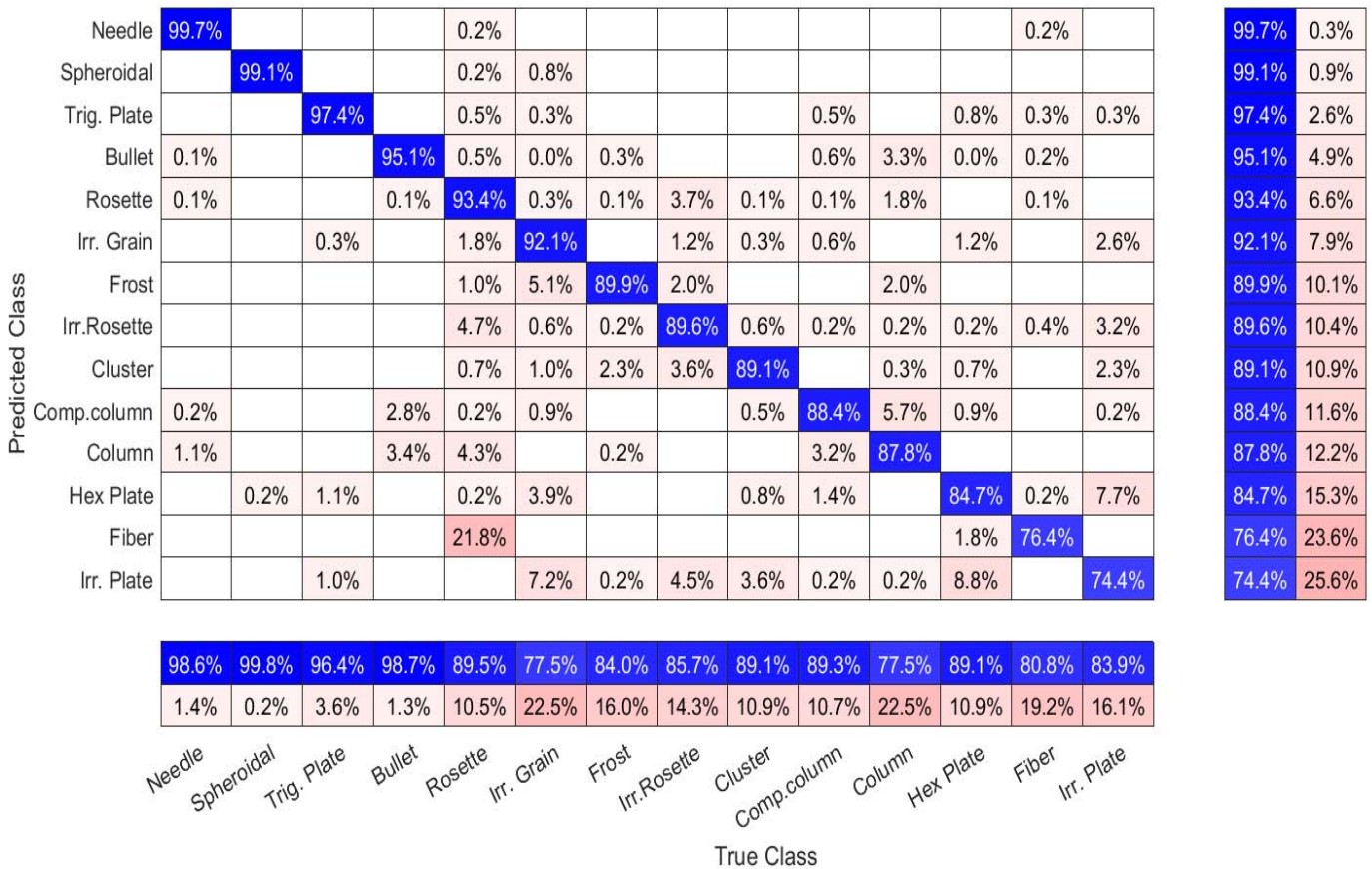
589 -Irregular grains are sometimes mistaken with irregular plates (10%) and hex plates (6%).

590 -Columns are misclassified as bullets 15% of the times.

591

592 The three-dimensional structure of the ice particles is lost in the ICE-CAMERA images, so that some thick ice forms such as
 593 C4a, P1b, G3b, CP1a, etc. (Kikuchi et al, 2013), if any, are likely to be misclassified by this CNN.

594 A different view to read the CNN test is the row-normalized summary of the confusion matrix (Fig. 20).



595

596 **Fig. 20: Confusion plot of the CNN – (row-normalized)**

597 Percentages along the i-th row now show the probability for a particle classified into the i-th class to effectively belong to
 598 each of the 14 true classes. Reading the rows of Fig. 20 from top to bottom, results are:

599 -Particles classified as needles, spheroidal, trigonal plates, bullets, pristine rosettes and irregular grains effectively (P>90%)
 600 belong to their class.

601 -Particles classified as irregular rosettes have a 5% chance of being regular rosettes

602 -Particles classified as compact columns have a 6% chance of being columns.

603 -Particles classified as columns have a 4% chance of being a 2-branch rosette and 3% of being bullets or compact columns.

604 -Particles classified as pristine plates have a 4% chance of being irregular grains.

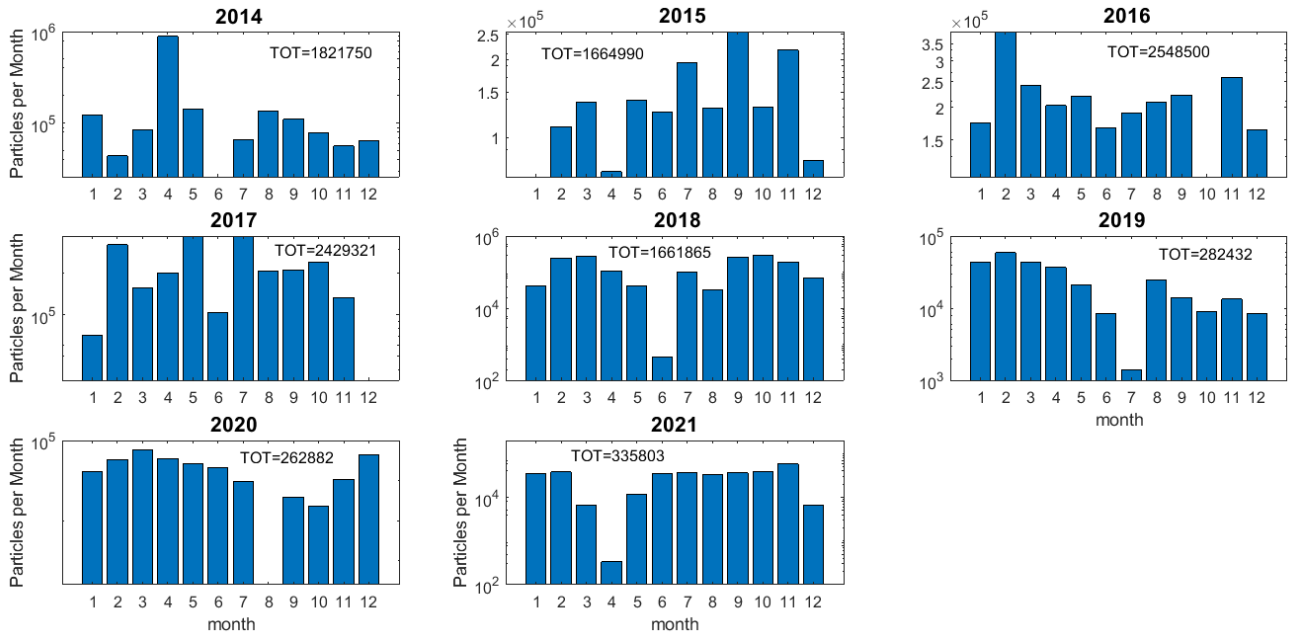
605 -Particles classified as irregular plates have a 7% chance of being irregular grains, 8% regular plates, and 5% of being
 606 irregular rosettes

607

608 **6.1 Overview of ICE-CAMERA data set.**

609 From January 2014 to December 2021, ICE-CAMERA has segmented a total of 11.007.543 particles. This gross count includes
610 particulates successively rejected for the statistical analysis. The distribution of the number of particles observed in the course
611 of the months is illustrated in Fig. 21. In some months, errors in ICE-CAMERA or processing software contributed to the
612 small numbers observed.

613



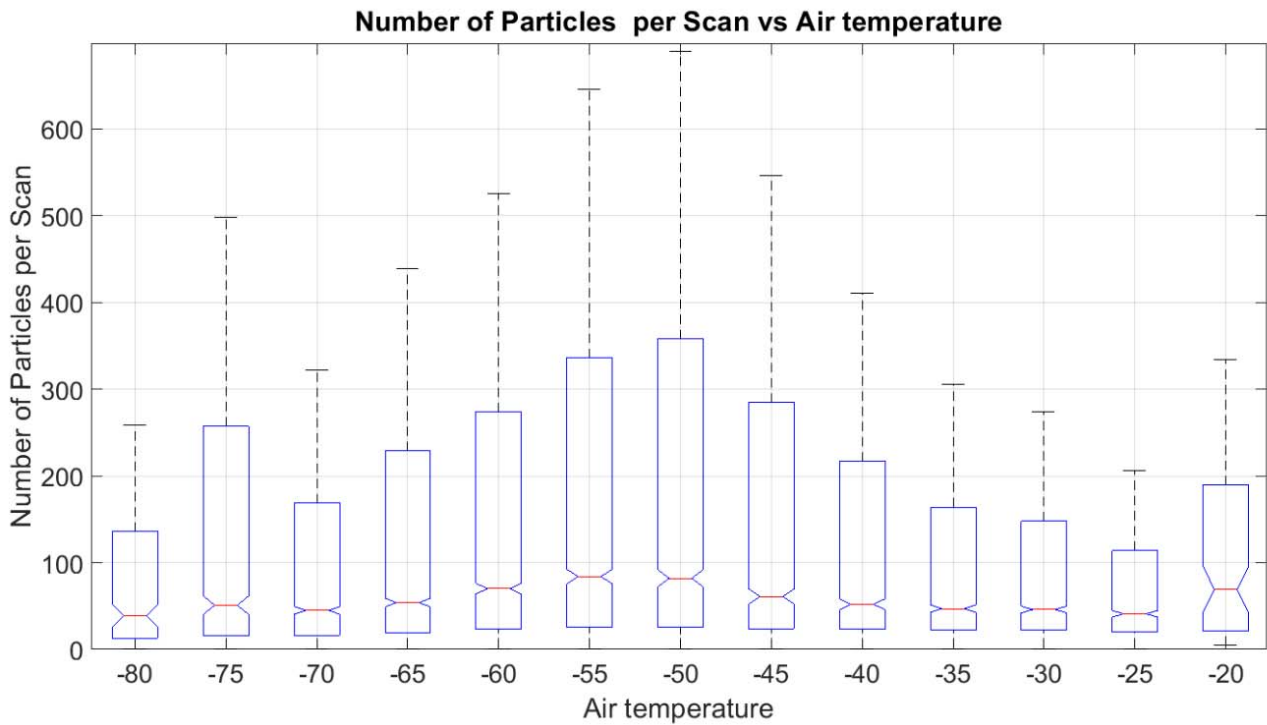
614

615 **Fig. 21: Ice particle count statistics per month for the years 2014 to 2021. The total number per-year is also indicated.**

616

617 The number of particles per scan (NpS) is a rough indicator of the intensity of the collected precipitation, but it could be
618 affected by sublimation, because in condition of 'warm' air the smallest particles could disappear from the DS before being
619 detected (sec.3.2). Figure 22 shows the NpS in relation to the air temperature for the whole period 2014-2021, in box and
620 whisker format. On each box, the middle mark indicates the median, and the lower and upper edges indicate the 25th and 75th
621 percentiles, respectively. The lower and upper whiskers indicate an interquartile below the 25th percentile and an interquartile
622 above the 75th percentile.

623 Most ice particles were detected at temperatures between -60°C and -45°C, characteristic temperatures in spring and autumn.
624 The NpS at -70°C is not statistically different from the NpS at -30°C. This result suggests that sublimation on the SD during
625 the deposition period is less important than the natural variability of precipitation in determining the number of particles
626 detected during the acquisition.



627

628

Fig. 22: Statistics of NpS as a function of air temperature for the period 2014-2021

629

630 The same consideration can be deduced when considering the statistics of NpS with relative humidity (Fig. 23). Most particles

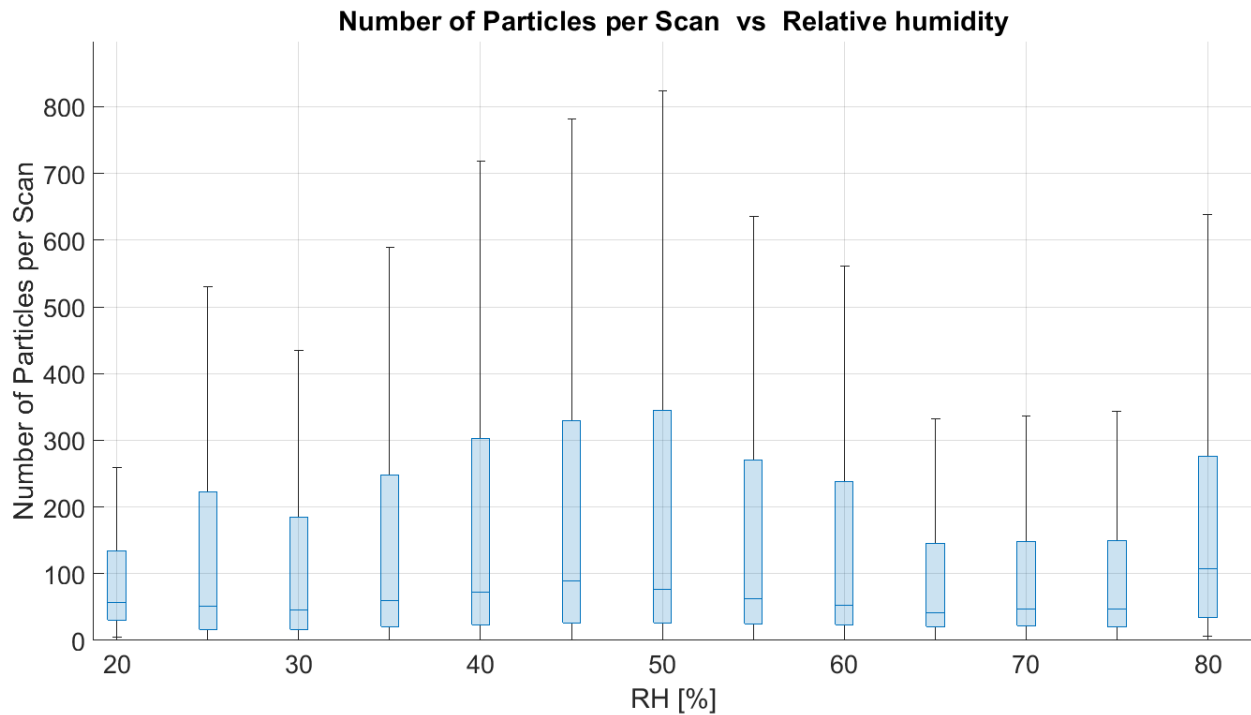
631 were detected with relative humidity ranging from 35% to 60%. NpS at 20% HR does not differ statistically from NpS at 80%

632 RH. Even if RH is less important than temperature in determining the sublimation rate, also this result suggests that

633 sublimation does not affect dramatically the number of particles finally detected by ICE-CAMERA.

634

635



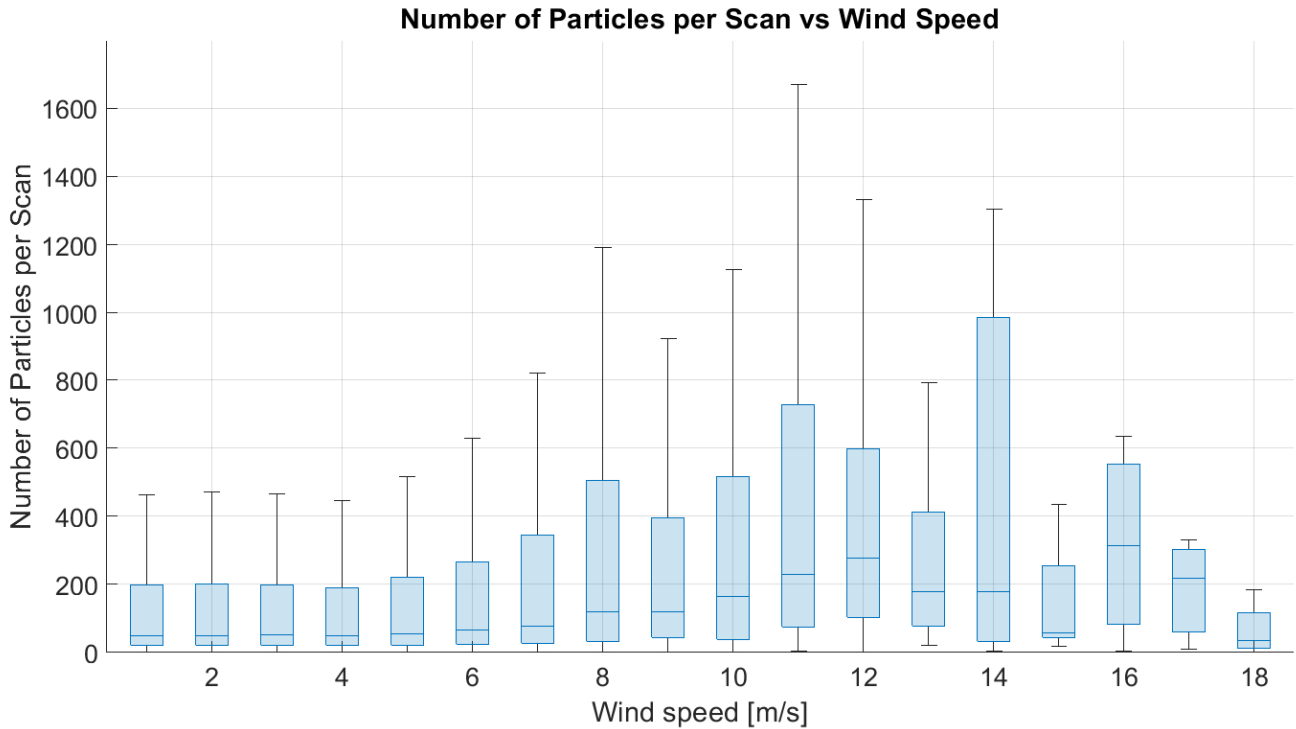
636

637

Fig. 23: NpS statistics based on RH for the period 2014-2021.

638

639 Figure 24 shows NpS in relation to wind velocity. Ice particles were collected by ICE-CAMERA under all wind velocity
 640 conditions encountered in DC. Ice particles were numerically more abundant when the wind was between 7 ms⁻¹ and 16 ms⁻¹.
 641 As the average surface wind speed at DC is around 3≈4 m s⁻¹, particles were collected on the DS preferentially with winds
 642 stronger than the average, a condition typically encountered in winter (Argentini et al.,2014). These winds exceed the threshold
 643 value of 5 m s⁻¹ for blowing snow at ICE-CAMERA altitude, and may ultimately contain drifting snow. The drop of NpS for
 644 the highest wind speeds (rare in DC) is probably due to the limited attachment of snow to the DS.
 645



646 **Fig. 24: NpS statistics in terms of wind speed for the period 2014-2021.**

648

649

650

651 **6.2 Image processing and CNN used on ICE-CAMERA data.**

652 MATLAB post-processing software, including the CNN classifier (Sect.4.2) and measurement tools (Sect.4.1) has been
 653 applied to the 2014-2017 ICE-CAMERA dataset. Even if the detailed analysis of these data is the task of a separate paper, a
 654 sample of the capacity of the instrument is presented in this section for the first two years of measurement (2014-2015). The
 655 total particles analyzed resulted in N=553.358. The number of particles classified in the 14 classes is reported in Fig. 25. The
 656 relative rarity of trigonal plates and spheroid particles is evident.

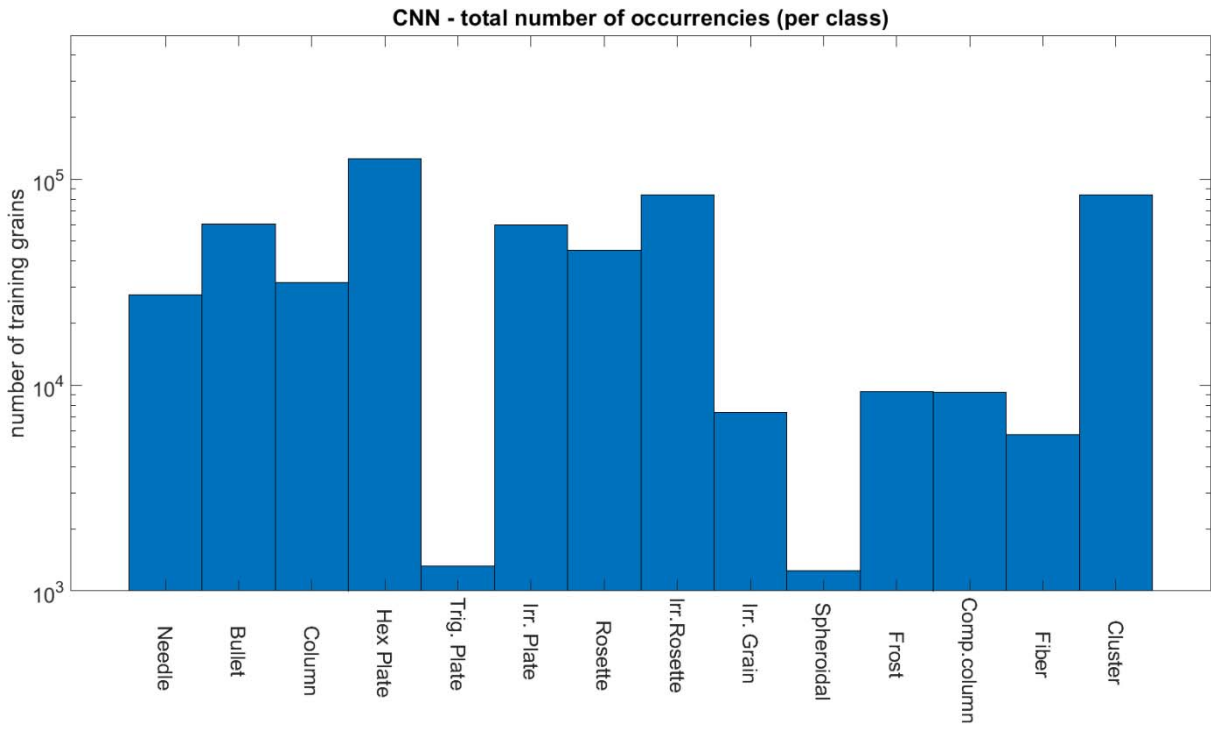


Fig. 25: Particles classified in the 14 classes for years 2014-2015 .

657

658

659

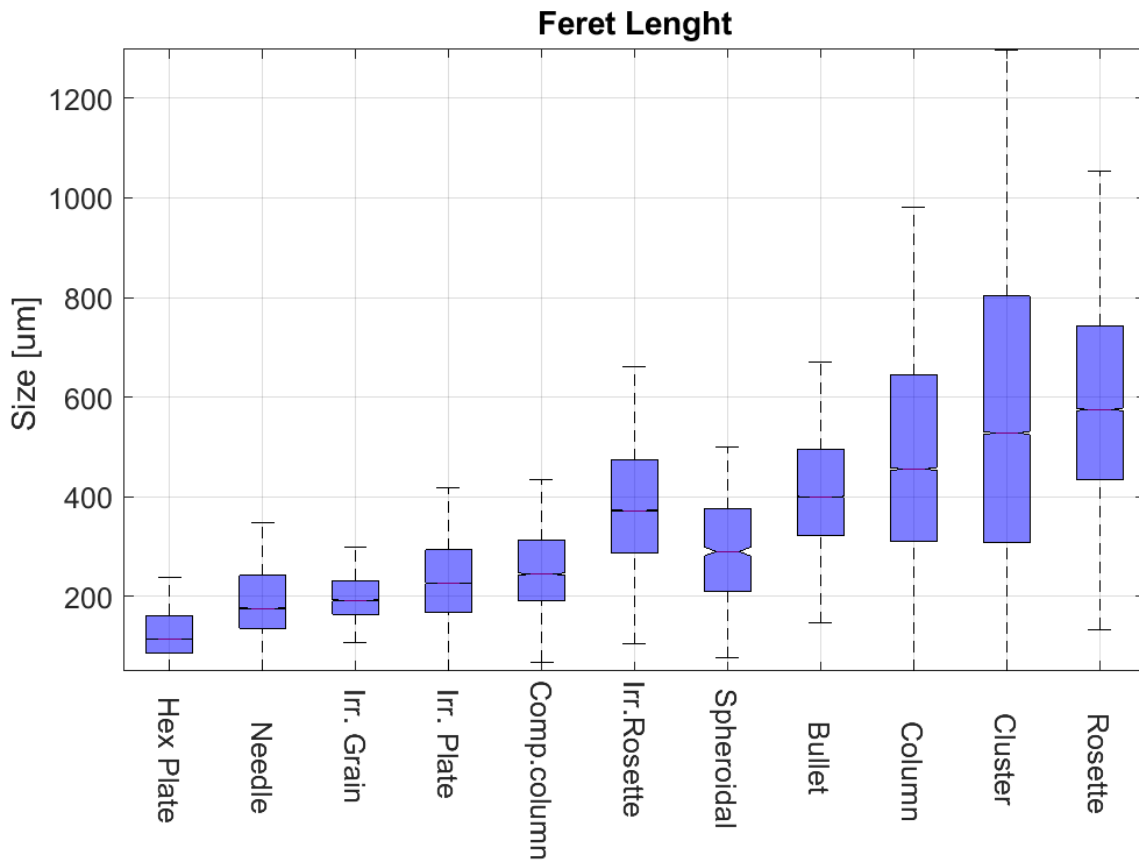
660 Figure 26 shows the Feret length statistics in box and whisker format. Particles classified as plates, needles, compact columns,
 661 spheroidal and irregular grains gave an average length lower than 300 μm . Bullets and columns mean length resulted in the
 662 400-500 μm range, while for rosettes and irregular rosettes was in the 350-550 μm range.

663

664

665

666

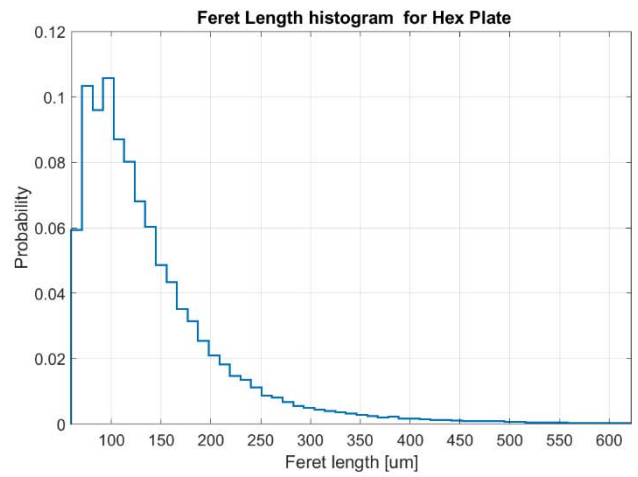
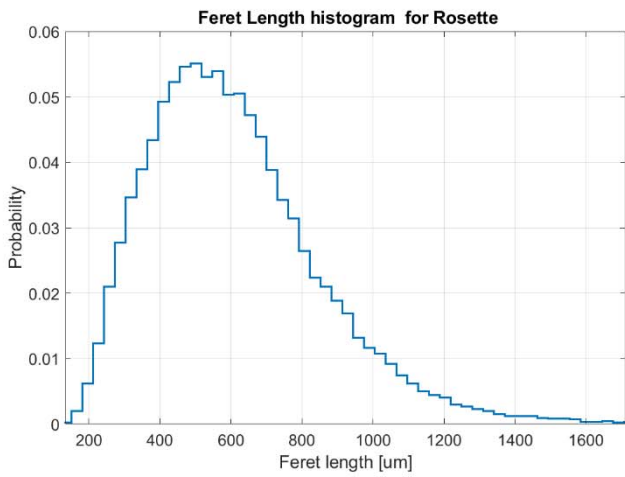


668

669

Fig. 26: Feret length statistics for the years 2014-2015

670 Figure 27 shows in detail the probability distribution of the Feret length for plates and rosettes. For plates, the peak of the
 671 distribution is for $L_{\text{feret}}=100 \mu\text{m}$, similar to the peak of the diamond dust (maximum) size distribution measured by Lawson
 672 et al. (2006) at SPS in summer. It must be pointed out that Lawson et al. (2006) measured also particles as small as $30 \mu\text{m}$,
 673 while particles below $60 \mu\text{m}$ are not processed by the ICE-CAMERA software, and are therefore missing from the probability
 674 distribution. This finding indicates that the possible sublimation of particles less than $100\text{-}200 \mu\text{m}$ during the deposition time,
 675 suggested in Section 3.2, is not relevant for the final particle size statistics. The results obtained from ICE-CAMERA for
 676 pristine rosettes differ considerably from those of Lawson et al (2006), because the peak of the probability distribution resulted
 677 $L=480 \mu\text{m}$, to be compared with $L=120 \mu\text{m}$ of Lawson et al (2006). This difference is not explicable with the eventual
 678 sublimation of the smallest rosettes on the DS. Instead, this result is a realistic feature, sustained by the direct visual observation
 679 of rosettes in DC precipitation.

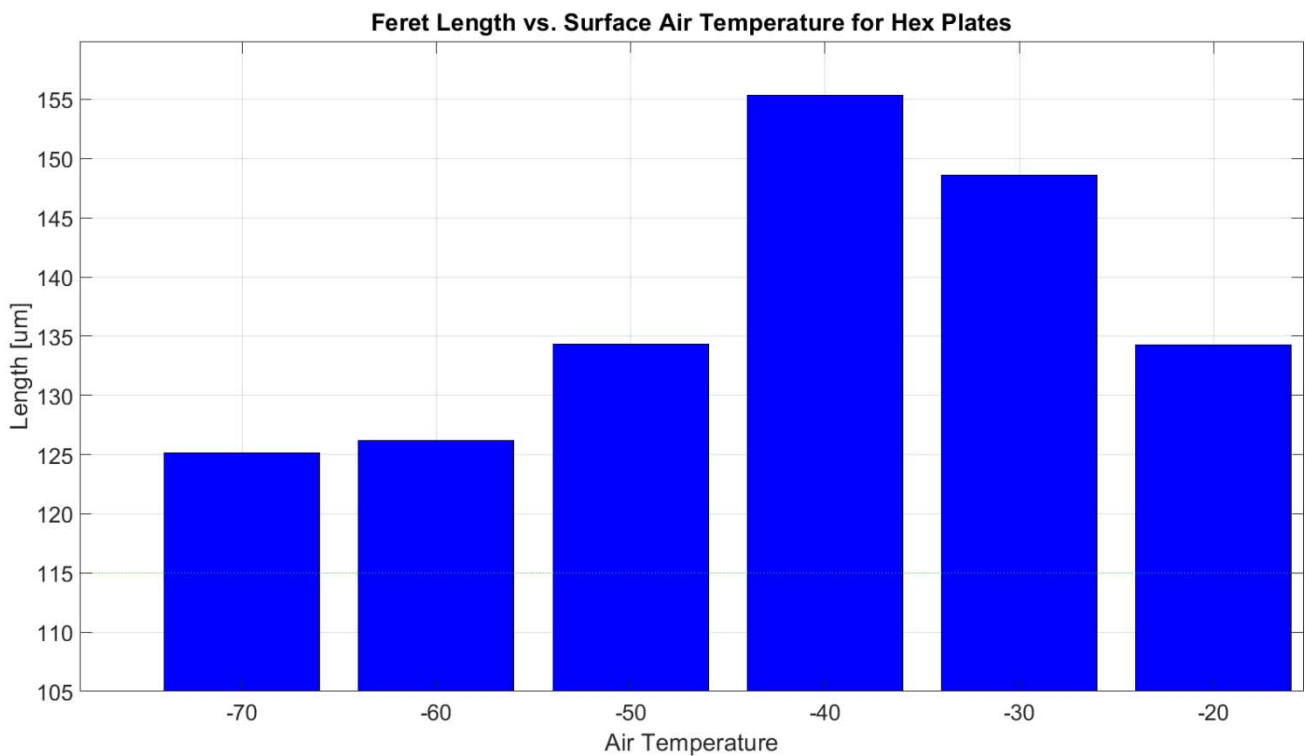


680

681 **Fig. 27: Feret length probability distribution for rosettes and regular plates. The important presence of small plates**
 682 **($D < 200 \mu\text{m}$) suggests that sublimation on the DS is not relevant. years 2014-2015**

683 **Figure 28 shows the trend of the mean Feret length of hexagonal plates with air temperature (sample size=121166 plates).**
 684 **The maximum plate size is observed at temperatures of -30 to -40°C. If sublimation on the DS dominated the size**
 685 **distribution of the plates observed after a DS scan, an inverse relationship between size and temperature would be expected.**
 686 **This finding again suggests that sublimation on the DS (even in summer, and up to -30°C air temperature) is not as important**
 687 **as numerical simulations might suggest.**

688

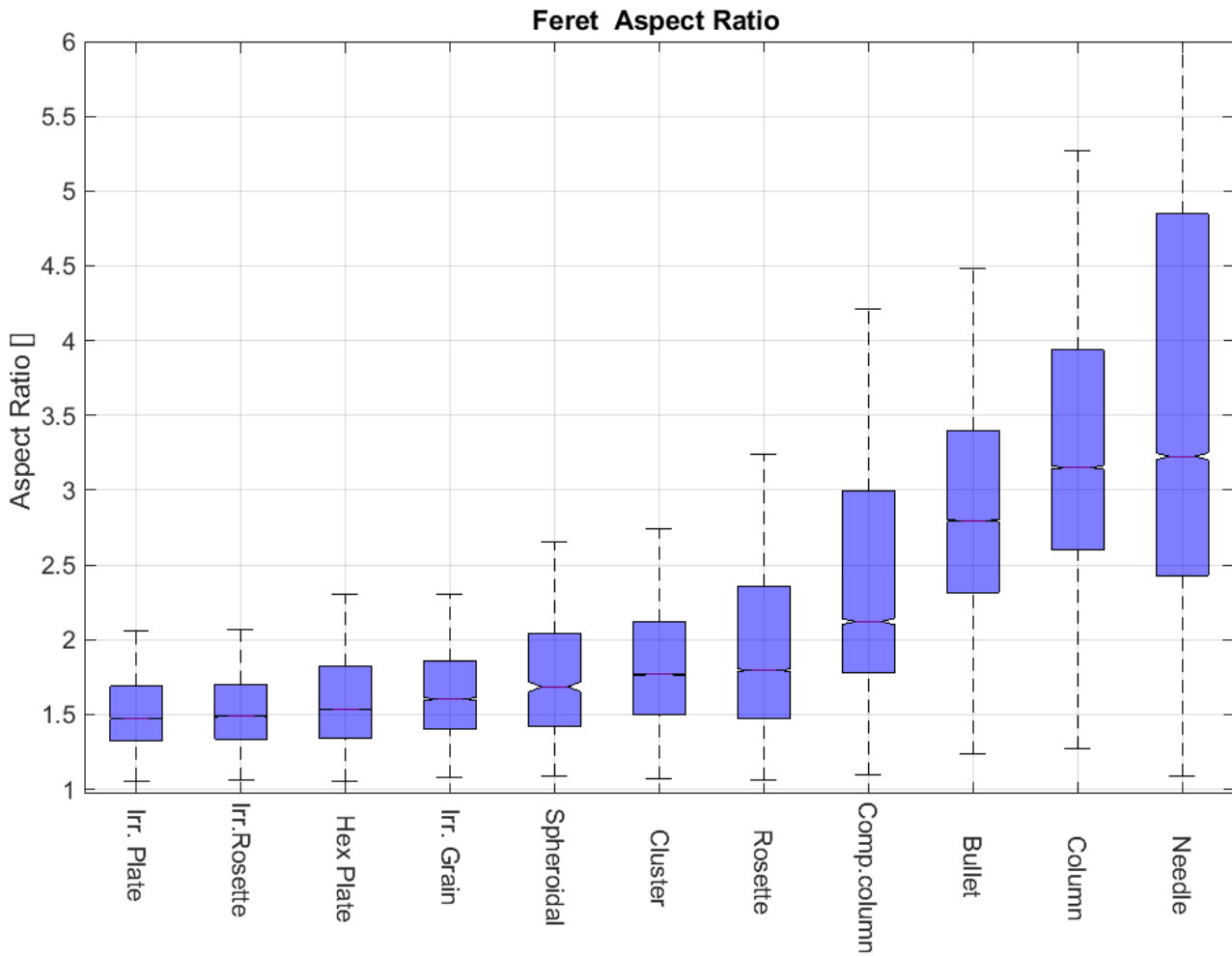


689

690 **Fig. 28: Average plate length with respect to air temperature – years 2014 to 2015.**

691

692 Figure 29 shows Feret's aspect ratio per class. Not surprisingly, many "rounded" classes (plates, rosettes, etc.) have an AR<2.
 693 Compact columns show a median AR close to 2.4, while columns and bullets are close to 3. The average AR for the needles
 694 was 3.2, which is lower than expected for the reasons outlined in section 4.1.4.



695

696

Fig. 29: Aspect Ratio statistics for the years 2014-2015

697

698 Figure 30 shows the surface-equivalent diameter D_s of the particles. Figure 31 shows the ratio between the surface equivalent
 699 diameter (D_s) and the bounding box equivalent diameter (D_f). The difference between the two diameters is relevant for "fluffy"
 700 particles like rosettes and clusters. For those particles, D_s/D_f gave values of 0.6 to 0.65. For comparison, a round particle is
 701 expected to have a ratio of $D_s/D_f=0.78$.

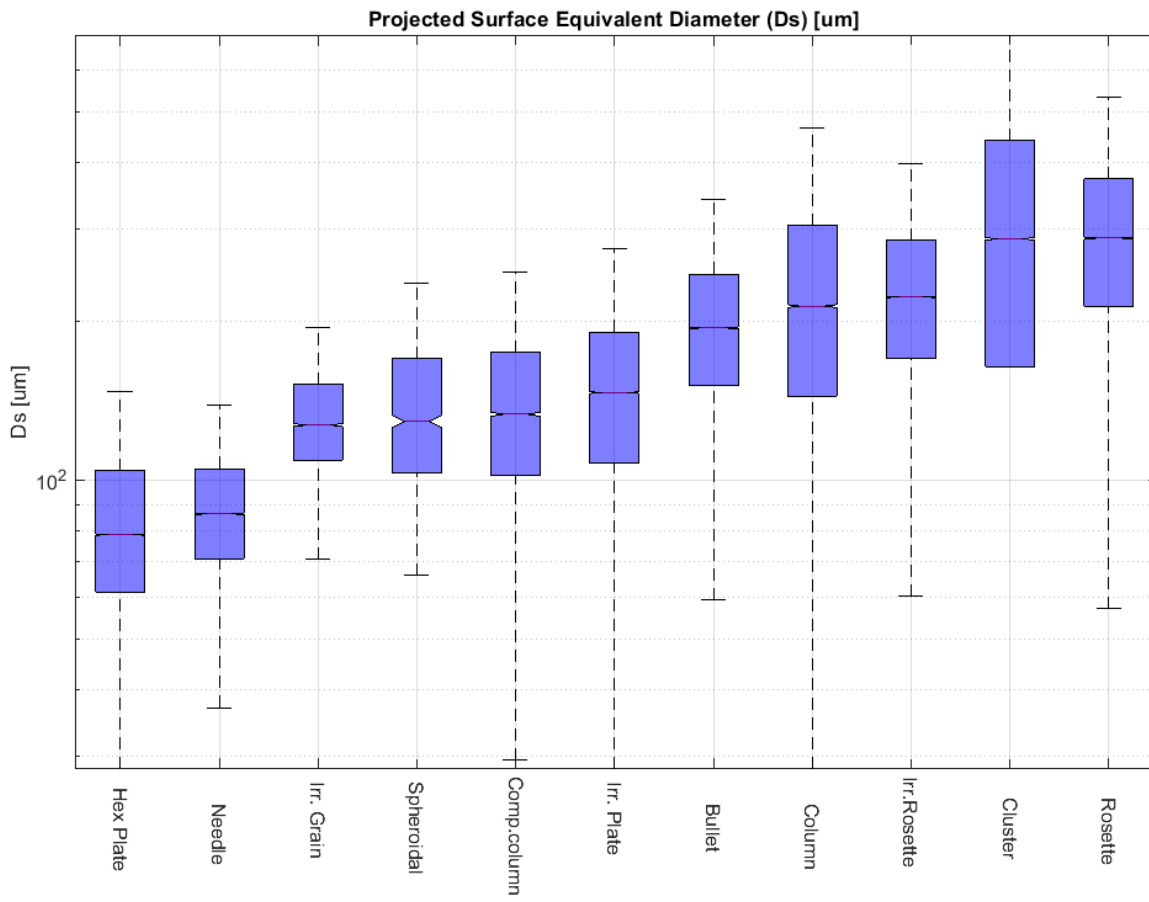


Fig. 30: Projected surface-equivalent diameter (Ds) for the years 2014-2015

702

703

704

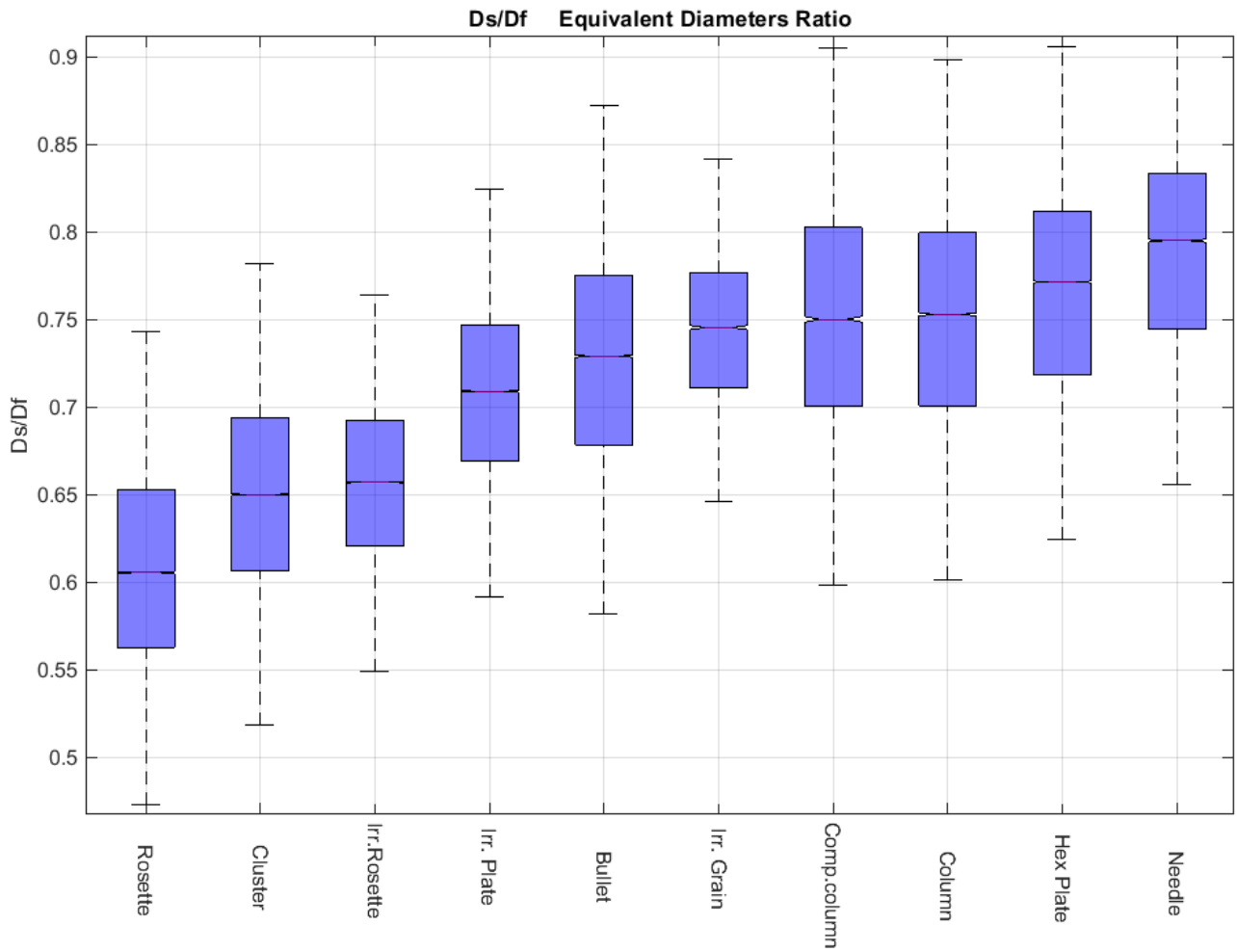


Fig. 31 Ratio between surface-equivalent (Ds) and Feret box-equivalent (Df) diameters - years 2014-2015

705

706

707

708

709

710

711

712

713

714

715

716

717

718

719

720

721

722 **6. Conclusions.**

723 ICE-CAMERA, although very similar to a simple flatbed scanner in its basic design, has represented a technical challenge for
724 its implementation at DC. Hardware and software have been continuously and extensively modified at DC over the past five
725 summer campaigns. The result is now a reliable instrument, running throughout the year on an hourly basis, for the statistical
726 study of precipitation in internal polar areas. Particle size and morphology are automatically obtained, and some semi-
727 quantitative precipitation estimates can be derived. The collected data are automatically pre-analyzed, but they can be post-
728 processed at any time, in order to follow the continuous improvements of the image processing and machine learning
729 algorithms. The GoogleNet CNN, trained specifically for this instrument, has succeeded in classifying ICE-CAMERA images
730 into 14 form classes, with an accuracy of more than 80% for most of them. The instrument is particularly useful for
731 automatically measuring the size of individual ice particles in precipitation, a process virtually impossible manually, and
732 certainly impossible on the field in DC and elsewhere on the Antarctic plateau in winter. ICE-CAMERA scans are carried out
733 every hour. Keeping the surface of the instrument free of frost all the time and cleaning it by heating the deposition surface
734 after each scan is paid with the possible loss of small ice particles. Particles less than 100-200 μm can disappear by sublimation
735 before being recorded, especially in summer. This problem is complementary to the problem encountered when observing
736 precipitation manually: when observing precipitation manually every 24 hours, (as is the case of DC) the reprocessing of
737 particles, or the formation of ice and hoar artifacts cannot be prevented. In ICE-CAMERA, frost and ice regrowth are
738 suppressed, but small particles may disappear for sublimation. ICE-CAMERA data, collected since 2014, have already been
739 statistically processed and the results will be described in a specialized paper. Results from a subset of data (years from 2014
740 to 2015), was presented in this work. These results demonstrated the capability of the instrument to classify and size individual
741 ice particles in DC precipitation, apparently without dramatic losses of small particles for sublimation. Cloud precipitation
742 particles (rosettes) were found to be significantly larger (480 μm) than those observed at SPS by Lawson et al (2006), while
743 plates resulted of similar size (120 μm). Unfortunately, only non-polluted, very cold, low humidity, low precipitation
744 environments (like high mountain tops, dry polar environments) could house a similar instrument. In the presence of pollution,
745 marine aerosols or dust, manual cleaning of the DS would be required to remove solid particles and salts escaping sublimation.
746 For coastal zones, the temperature is generally close to zero, making the thermal cleaning of the DS by sublimation
747 problematic. In these environments, if an instrument like ICE-CAMERA were installed, a mechanical wiper would replace the
748 heated window of the current instrument. Furthermore, the CNN presented in this paper should be re-trained with different
749 classes of ice crystals.

750

751 **7. Technical issues.**

752 Using ICE-CAMERA at DC, as well as other automated instruments, was difficult. The instrument had several failures along
753 years, and each one was difficult to fix, at least in winter, when the instrument had to be dismantled from the roof of the
754 shelter at -70°C and eventually fixed in the local lab by the winter-over crew, with remote assistance from Europe. Until a few
755 years ago, communicating with DC was limited to email with small attachments, making remote assistance a lengthy task.
756 Even today, connecting the rest of the world remotely with the ICE-CAMERA PC, to operate on the instrument software, is
757 virtually impossible. Most hardware failures in DC were due to software bugs or computer failures. Rather than having trouble
758 with low temperatures, operating in DC means dealing with limited heat-dissipation of PC parts such as power supply and
759 hard disks, electrostatic discharge issues in low-humidity, heated environments, lack of spare parts for most of the year, a
760 variable skill-ness of winter-over personnel. Failures in the thermal control of ICE-CAMERA caused some mechanical stress
761 and failures in the focusing sledge, while water condensation eventually rusted the bearings of the stepper motors (all bearing
762 were de-greased for a better low temperature operation). The CNN used to classify ICE-CAMERA images is continually
763 changing and improving and the CNN training data set increases with time, as new images collected by ICE-CAMERA are
764 used as new training ones.

765

766

767 **Code and Data availability.**

768 The CNN developed as part of this work (under Mathworks MATLAB R2020B), along with the image data set (224*224
769 images for the 14 classes of particles) used for training, validation and testing the CNN are available at ZENODO repository
770 (Del Guasta, 2022)

771

772

773

774 **Acknowledgements.**

775 I am grateful to the Italian Antarctic Project PNRA for supporting this work with the projects ICE-CAMERA (PNRA
776 2009/A4.1) and PRE-REC (PNRA 2013/AC3.05). I am also grateful to the ‘Osservatorio Meteo-Climatologico Antartico’
777 (PNRA 14_00100) for the Meteo data, and to all the logistics staff and winter-over crews of Concordia station, all working
778 hard to permit our scientific activity. I am also grateful to Francesco Castagnoli (INO CNR) for the initial design of the
779 instrument.

780

781

782

783 **References.**

784 Aristidi, E.: An analysis of temperatures and wind speeds above Dome C, Antarctica, *Astronomy and Astrophysics*, 430, 739–
785 746, <https://doi.org/10.1051/0004-6361:20041876>, 2005.

786 Argentini, S., Pietroni, I., Mastrantonio, G., P., V. A., Dargaud, G., and Petenko, I.: Observations of near surface wind speed,
787 temperature and radiative budget at Dome C, Antarctic Plateau during 2005, *Antarct. Sci.*, 26(1), 104–112,
788 <https://doi.org/10.1017/S0954102013000382>, 2014.

789

790 Bailey, M.P. , Hallett, J.: A Comprehensive Habit Diagram for Atmospheric Ice Crystals: Confirmation from the
791 Laboratory, AIRS II, and Other Field Studies, *J..Atm..Sci.*, 61, 2888–2899, <https://doi.org/10.1175/2009JAS2883.1>, 2009.

792 Bracci, A., Baldini, L., Roberto, N., Adirosi, E., Montopoli, M., Scarchilli, C., Grigioni, P., Ciardini, V., Levizzani, V., Porcù,
793 F.: Quantitative Precipitation Estimation over Antarctica Using Different $Ze-SR$ Relationships Based on Snowfall
794 Classification Combining Ground Observations. *Remote Sens.* 2022, 14, 82. <https://doi.org/10.3390/rs14010082>, 2022.

795

796 Bromwich, D. H.: Snowfall in high southern latitudes, *Rev. Geophys.*, 26(1), 149–168,
797 <https://doi.org/10.1029/RG026i001p00149>, 1988.

798 Del Guasta, M.: CNN for the classification of ICE-CAMERA images of Antarctic ice particles, Zenodo [code],
799 <https://doi.org/10.5281/zenodo.6822140>, 2022.

800

801 Deng, J., Dong, W., Socher, R., Li, L.-J., Li, K., and Li, F.-F.: ImageNet: A large-scale hierarchical image database, *IEEE*
802 *Conference on Computer Vision and Pattern Recognition*, 248–255, <https://doi.org/10.1109/CVPR.2009.5206848>, 2009.

803

804 Eidevåg, T., Abrahamsson, P., Eng, M., and Rasmuson, A.: Modeling of dry snow adhesion during normal impact with surfaces,
805 *Powder Technology*, 361, 1081–1092, <https://doi.org/10.1016/j.powtec.2019.10.085>, 2020

806

807 Fujita, K., Abe, O.: Stable isotopes in daily precipitation at Dome Fuji, East Antarctica, *Geophys. Res. Lett.*, 33, L18503,
808 <https://doi.org/10.1029/2006GL026936>, 2006.

809

810 Garrett, T. J., Fallgatter, C., Shkurko, K., Howlett, D.: Fall speed measurement and high-resolution multi-angle photography
811 of hydrometeors in free fall, *Atmos. Meas. Tech.*, 5, 2625–2633, <https://doi.org/10.5194/amt-5-2625-2012>, 2012

812

813 Genthon, C., Six, D., Gallée, H., Grigioni, P., Pellegrini, A.: Two years of atmospheric boundary layer observations on a 45-
814 m tower at Dome C on the Antarctic plateau, *J. Geophys. Res. Atmos.*, 118, 3218– 3232, <https://doi.org/10.1002/jgrd.50128>,
815 2016

816

817 Genthon, C., Veron, D. E., Vignon, E., Madeleine, J.-B., Piard, L.: Water vapor in cold and clean atmosphere: a 3-year data
818 set in the boundary layer of Dome C, East Antarctic Plateau, *Earth Syst. Sci. Data*, 14, 1571–1580,
819 <https://doi.org/10.5194/essd-14-1571-2022>, 2022.

820

821 Grazioli, J., Tuia, D., Monhart, S., Schneebeli, M., Raupach, T., and Berne, A.: Hydrometeor classification from two-
822 dimensional video disdrometer data, *Atmos. Meas. Tech.*, 7, 2869–2882, <https://doi.org/10.5194/amt-7-2869-2014>, 2014.

823

824 Grazioli, J., Genthon, C., Boudevillain, B., Duran-Alarcon, C., Del Guasta, M., Madeleine, J.-B. and Berne, A.: Measurements
825 of precipitation in Dumont d'Urville, Adélie Land, East Antarctica, *The Cryosphere*, 11, 1797–1811,
826 <https://doi.org/10.5194/tc-11-1797-2017>, 2017.

827

828 Grazioli, J., Madeleine, J.B., Gallée, H., Forbes, R.M, Genthon, C., Krinner, G., Berne, A. Katabatic Winds Diminish
829 Precipitation Contribution to the Antarctic Ice Mass Balance. *PNAS*, <https://doi.org/10.1073/pnas.1707633114>, 2017.

830

831 Ham, F.S.: Shape-preserving solutions of the time-dependent diffusion equation, *Quart. Appl. Math.* 17, 137-145
832 <https://doi.org/10.1090/qam/108196>, 1959.

833

834 Heymsfield, A. J., Protat, A., Bouniol, D., Austin, R. T., Hogan, R. J., Delanoë, J., Okamoto, H., Sato, K., van Zadelhoff, G.,
835 Donovan, D. P., Wang, Z.: Testing IWC Retrieval Methods Using Radar and Ancillary Measurements with In Situ
836 Data, *Journal of Applied Meteorology and Climatology*, 47(1), 135-163. Retrieved Jun 28, 2022,
837 <https://doi.org/10.1175/2007JAMC1606.1>, 2008.

838

839 Hiley, M. J. , Kulie, M.S., Bennartz R.: Uncertainty Analysis for CloudSat Snowfall Retrievals, *Journal of Applied*
840 *Meteorology and Climatology*, 50, 2 ,399-418, 2011.

841

842 Hogan, A. W.: Summer Ice Crystal Precipitation at the South Pole. ,*J. of Appl. Meteorol.*, 14, 2, 246-248,
843 [https://doi.org/10.1175/1520-0450\(1975\)014<0246:SICPAT>2.0.CO;2](https://doi.org/10.1175/1520-0450(1975)014<0246:SICPAT>2.0.CO;2), 1975.

844

845 Huffman, G. J., Adler, R. F., Morrissey, M. M., Bolvin, D. T., Curtis, S., Joyce, R., McGavock, B., Susskind, J.: Global
846 Precipitation at One-Degree Daily Resolution from Multisatellite Observations. *Journal of Hydrometeorology* 2, 1, 36-50,
847 <https://doi.org/10.1175/1525>, 2001.

848

849 Hu, MK.: Visual pattern recognition by moment invariants, *Information Theory, IRE Transactions*, 8, 179-187,
<https://doi.org/10.1109/TIT.1962.1057692>, 1962.

850 Jambon-Puillet, E., Shahidzadeh, N. and Bonn, D.: Singular sublimation of ice and snow crystals. *Nature Commun.* 9, 4191.
851 <https://doi.org/10.1038/s41467-018-06689-x>, 2018.

852 Kikuchi, K., Hogan A.W.: Properties of Diamond Dust Type Ice Crystals Observed in Summer Season at Amundsen-Scott
853 South Pole Station, Antarctica, *J. of the Meteorol. Soc. of Japan. Ser. II*, 57, 2, 180-
854 190, https://doi.org/10.2151/jmsj1965.57.2_180, 1979.

855 Kikuchi, K., Kameda, T., Higuchi, K., Yamashita, A.: A global classification of snow crystals, ice crystals, and solid
856 precipitation based on observations from middle latitudes to polar regions, *Atmos. Res.*,132,460–472,
857 <https://doi.org/10.1016/j.atmos.res.2013.06.006>, 2013.
858

859 Konishi H., Muramoto K., Shiina T., Endoh T., Kitano K.: Z-R relation for graupels and aggregates observed at Syowa
860 station, Antarctica. *Proc. NIPR Symp. Polar Meteorol. Glaciol.*,5 ,97-103,1992.

861

862 Lachlan-Cope, T., Ladkin, R., Turner, J., & Davison, P. :Observations of cloud and precipitation particles on the Avery Plateau,
863 Antarctic Peninsula. *Antarctic Science*, 13(3), 339-348. <https://doi.org/10.1017/S0954102001000475>,2001

864 Lamb, D.,Hobbs, P. V.: Growth Rates and Habits of Ice Crystals Grown from the Vapor Phase, *Journal of Atmospheric*
865 *Sciences*, 28(8), 1506-1509, [https://doi.org/10.1175/1520-0469\(1971\)028<1507:GRAHOI>2.0.CO;2](https://doi.org/10.1175/1520-0469(1971)028<1507:GRAHOI>2.0.CO;2), 1971.

866 Lawson, R. P., Baker, B. A., Zmarzly, P., O'Connor, D., Mo, Q., Gayet, J., Shcherbakov, V. Microphysical and Optical
867 Properties of Atmospheric Ice Crystals at South Pole Station, *Journal of Applied Meteorology and Climatology*, 45(11),
868 1505-1524. <https://doi.org/10.1175/JAM2421.1>, 2006.

869 LeCun, Y., Bengio, Y., Hinton, G.: Deep learning. *Nature* ,521, 436–444, <https://doi.org/10.1038/nature14539>, 2015.
870

871 Libbrecht ,K.G.: The physics of snow crystals. *Rep. Prog. Phys.*, 68, 855–895, <https://doi.org/10.1088/0034-4885/68/4/R03>,
872 2005.
873

874 Libbrecht, K.G.: Physical Dynamics of Ice Crystal Growth. *Annual Review of Materials Research*. 47.
875 <https://doi.org/10.1146/annurev-matsci-070616-124135>, 2017.
876

877 Libois, Q., Picard, G., Arnaud, L., Morin, S., and Brun, E.: Modeling the impact of snow drift on the decameter-scale
878 variability of snow properties on the Antarctic Plateau, *J Geophys Res Atmos*, 119, 662–681,
879 <https://doi.org/10.1002/2014JD022361>, 2014.
880

881 Lindqvist, H., Muinonen, K., Nousiainen, T., Um, J., McFarquhar, G. M., Haapanala, P., Makkonen, R. and Hakkarainen,
882 H. : Ice-cloud particle habit classification using principal components, *J. Geophys. Res.*, 117, D16206,
883 <https://doi.org/10.1029/2012JD017573>, 2012.
884

885 Liu, G.,Deriving snow cloud characteristics from cloudsat observations,*J. Geophys. Res. Atmos.*, 113 , D00A09,
886 <https://doi.org/10.1029/2007JD009766>, 2008.
887

888 Magono, C., Lee, C. W.: Meteorological classification of natural snow crystals. *J. of the Faculty of Sci., Hokkaido*
889 *University. Series 7, Geophysics*, 2(4), 321-335, 1966.

890

891 Nelson, J.: Sublimation of Ice Crystals, *Journal of the Atmospheric Sciences*, 55(5), 910-919. [https://doi.org/10.1175/1520-](https://doi.org/10.1175/1520-0469(1998)055<0910:SOIC>2.0.CO;2)
892 [0469\(1998\)055<0910:SOIC>2.0.CO;2](https://doi.org/10.1175/1520-0469(1998)055<0910:SOIC>2.0.CO;2), 1988.

893

894 Ohtake, T. and Yogi T.: Winter ice crystals at the South Pole. *Antarct. J. U.S.*, 14, 201–203, 1979.

895

896 **Palerme, C., Kay, J. E., Genthon, C., L'Ecuyer, T., Wood, N. B., and Claud, C.: How much snow falls on the Antarctic ice**
897 **sheet?, *The Cryosphere*, 8, 1577–1587, <https://doi.org/10.5194/tc-8-1577-2014>, 2014.**

898

899 **Palerme, C., Claud C., Dufour, A., Genthon, C., Wood N. B., L'Ecuyer, T.: Evaluation of Antarctic snowfall in global**
900 **meteorological reanalyses, *Atmospheric Research*, 190, 104-112, <https://doi.org/10.1016/j.atmosres.2017.02.015>, 2017.**

901

902 Pratt, W. K.: *Digital Image Processing: PIKS Scientific Inside*, Fourth Edition, John Wiley & Sons, Inc., Los Altos,
903 California, <https://doi.org/10.1002/0470097434>, 2006.

904

905 **Praz, C., Roulet, Y.-A., and Berne, A.: Solid hydrometeor classification and riming degree estimation from pictures collected**
906 **with a Multi-Angle Snowflake Camera, *Atmos. Meas. Tech.*, 10, 1335–1357, <https://doi.org/10.5194/amt-10-1335-2017>,**
907 **2017.**

908

909 **Ryzhkin I. A., Petrenko V. F., Physical Mechanisms Responsible for Ice Adhesion, *J. Phys. Chem. B* 1997, 101, 32, 6267–6270,**
910 **<https://doi.org/10.1021/jp9632145>, 1977.**

911

912 Russ, J. C. and Brent Neal, F.: *The Image Processing Handbook* 7th Edition, CRC Press, pp 1053,
913 <https://doi.org/10.1201/b18983>, 2017.

914

915 Santachiara, G., Belosi, F., Prodi, F.: Ice crystal precipitation at Dome C site (East Antarctica), *Atmos. Res.* 167, 108-117,
916 <https://doi.org/10.1016/j.atmosres.2015.08.006>, 2016.

917

918 **Satow, K.: Observations on the Shapes of Snow Crystals in the Summer Season in Mizuho Plateau, Antarctica, *Memoirs of***
919 **National Institute of Polar Research. Special issue, 29, 103-109, 1983.**

920 Schlosser, E., Dittmann, A., Stenni, B., Powers, J. G., Manning, K. W., Masson-Delmotte, V., Valt, M., Cagnati, A.,
921 Grigioni, P., Scarchilli, C.: The influence of the synoptic regime on stable water isotopes in precipitation at Dome C, East
922 Antarctica, *The Cryosphere*, 11, 2345–2361, <https://doi.org/10.5194/tc-11-2345-2017>, 2017.

923 Schmidhuber, J.: Deep Learning in Neural Networks: An Overview. *Neural Networks*, 61, 85-
924 117, <https://doi.org/10.1016/j.neunet.2014.09.003>, 2014.

925

926 **Schneider, U., Finger, P., Meyer-Christoffer, A., Rustemeier, E., Ziese, M., Becker, A.: Evaluating the Hydrological Cycle**
927 **over Land Using the Newly-Corrected Precipitation Climatology from the Global Precipitation Climatology Centre**
928 **(GPCC). *Atmosphere* 2017, 8, 52. <https://doi.org/10.3390/atmos8030052>, 2017.**

- 930 Shorten, C., Khoshgoftaar, T.M.: A survey on Image Data Augmentation for Deep Learning. *J Big Data* 6, 60,
931 <https://doi.org/10.1186/s40537-019-0197-0>, 2019.
- 932 Shimizu, H., “Long prism” crystals observed in the precipitation in Antarctica. *J. Meteor. Soc. Japan*, **41**, 305–307.
933 https://doi.org/10.2151/jmsj1923.41.5_305, 1963.
- 934
- 935 Smiley, V. N., Whitcomb, B. M., Morley, B. M., & Warburton, J. A.: Lidar Determinations of Atmospheric Ice Crystal
936 Layers at South Pole during Clear-Sky Precipitation. *Journal of Applied Meteorology*, 19,9, 1074–1090, 1980.
- 937
- 938 Souverijns, N., Gossart, A., Lhermitte, S., Gorodetskaya I. V., Kneifel, S., Maahn, M., Bliven, F. L., van Lipzig, P. M.: Estimating
939 radar reflectivity - Snowfall rate relationships and their uncertainties over Antarctica by combining disdrometer and radar
940 observations, *Atmospheric Research*, 196, 211-223, <https://doi.org/10.1016/j.atmosres.2017.06.001>, 2017.
- 941 Szegeedy, C., Liu, W., Jia, Y., Sermanet P., Reed S., Anguelov D., Erhan D., Vanhoucke V. and Rabinovich A.: "Going
942 deeper with convolutions," 2015 IEEE Conference on Computer Vision and Pattern Recognition (CVPR), 1-9,
943 <https://doi.org/10.1109/CVPR.2015.7298594>, 2015.
- 944 Tremblin, P., Minier, V., Schneider, N., Durand, G. A., Ashley, M. C. B., Lawrence, J. S., Luong-Van, D. M., Storey,
945 J. W. V., Durand, G. A., Reinert, Y., Veyssiere, C., Walter, C., Ade, P., Calisse, P. G., Challita, Z., Fossat, E.,
946 Sabbatini, L., Pellegrini, A., Ricaud, P., Urban, J.: Site testing for submillimetre astronomy at Dome C, Antarctica, *A&A*
947 **535 A112**, <https://doi.org/10.1051/0004-6361/201117345>, 2011.
- 948 Vignon, E., Genthon, C., Barral, H., Amory, C., Picard, G., Gallée, H., Casasanta, G., and Argentini, S.: Momentum and heat
949 flux parametrization at Dome C, Antarctica: a sensitivity study, *Boundary-Layer Meteorol*, 162, 341–367,
950 <https://doi.org/10.1007/s10546-016-0192-3>, 2016.
- 951 Vignon, E., Genthon, C., Barral, H., Amory, C., Picard, G., Gallée, H., Casasanta, G., Argentini, S.: Momentum- and Heat-
952 Flux Parametrization at Dome C, Antarctica: A Sensitivity Study. *Boundary-Layer Meteorology*. [https://doi.org/](https://doi.org/10.1007/s10546-016-0192-3)
953 [10.1007/s10546-016-0192-3](https://doi.org/10.1007/s10546-016-0192-3), 2017.
- 954 Walden, V. P., Warren, S. G., Tuttle, E. (2003). Atmospheric Ice Crystals over the Antarctic Plateau in Winter, *Journal of*
955 *Applied Meteorology*, 42(10), 1391-1405, [https://doi.org/10.1175/1520-0450\(2003\)042<1391:AICOTA>2.0.CO;2](https://doi.org/10.1175/1520-0450(2003)042<1391:AICOTA>2.0.CO;2), 2003.
- 956 Walton, W.: Feret's Statistical Diameter as a Measure of Particle Size, *Nature*, **162**, 329–330,
957 <https://doi.org/10.1038/162329b0>, 1948.
- 958
- 959 Xiao, H., Zhang, F., He, Q., Liu, P., Yan, F., Miao, L. and Yang, Z.: Classification of ice crystal habits observed from airborne
960 Cloud Particle Imager by deep transfer learning., *Earth and Space Science*, 1877–1886, <https://doi.org/10.1029/2019EA000636>,
961 2019.
- 962
- 963 Wood, N., L'Ecuyer, T., Heymsfield, A., Stephens, G.: Microphysical Constraints on Millimeter-Wavelength Scattering
964 Properties of Snow Particles. *Journal of Applied Meteorology and Climatology*. 54. 909-931. [https://doi.org/10.1175/JAMC-](https://doi.org/10.1175/JAMC-D-14-0137.1)
965 [D-14-0137.1](https://doi.org/10.1175/JAMC-D-14-0137.1), 2015.

966

967 Zheleznyak, A.G. , Sidorov, V.G.: Flatbed scanner as an instrument for physical studies, St. Petersburg Polytechnical

968 University Journal: Physics and Mathematics, 1, Issue 2, 134-141, <https://doi.org/10.1016/j.spjpm.2015.04.001>. 2015.

969